Loss of coiled-coil protein Cep55 impairs abscission processes and results in p53-dependent apoptosis in developing cortex

Jessica N. Little[1,3*], Katrina C. McNeely[1*], Nadine Michel[2,3]Christopher J. Bott[1], Kaela S. Lettieri[1], Madison R. Hecht[1], Sara A. Martin[1] and Noelle D. Dwyer[1#]

*co-first author

[1]Department of Cell Biology, and [2]Department of Biochemistry and Molecular Genetics, and [3]Medical

Scientist Training Program, University of Virginia School of Medicine, Charlottesville, VA, USA

#author for correspondence: ndwyer@virginia.edu

Abstract

To produce a brain of normal size and structure, embryonic neural stem cell (NSCs) must tightly regulate

their cell divisions. Cerebral cortex NSCs undergo a polarized form of cytokinesis whose regulation is

poorly understood. Cytokinetic abscission severs the daughter cells and is mediated by the midbody at the

apical membrane. Here we elucidate the role of the coiled-coil midbody protein Cep55 in NSC abscission

and brain development. A knockout of Cep55 in mice causes microcephaly with reduced NSCs and

neurons, but relatively normal body size. Fixed and live analyses show NSCs lacking Cep55 have

decreased but not eliminated ESCRT recruitment, and have abnormal abscission and higher rates of

failure. P53-mediated apoptosis is greatly increased in the brain, but not other tissues, and p53 knockout

partly rescues brain size. Thus, loss of Cep55 causes abscission defects and failures in multiple cell types,

but the secondary p53 response and apoptosis is brain-specific.

Introduction

Embryonic neural stem cells (NSCs) must undergo rapid divisions within strict developmental

time windows to produce numerous daughter cells of various fates, to build a brain of correct size and

structure. They do so within a polarized epithelium, with their apical membranes forming the ventricle

wall, and their basal processes contacting the pia. Their nuclei move to the apical membrane for mitosis

and cytokinesis. We previously showed cytokinesis in NSCs is polarized and developmentally regulated

(McNeely & Dwyer, 2020). The cleavage furrow ingresses asymmetrically, forming the midbody within

the apical membrane. The midbody then mediates severing of the intercellular bridge, in a process called

abscission. Errors in cytokinesis are one etiology of microcephaly, in which the brain is

disproportionately small relative to body size (Bondeson et al., 2017; Di Cunto et al., 2000; Frosk et al.,

2017; Li et al., 2016; Makrythanasis et al., 2018; Moawia et al., 2017). We previously showed mutation

37 of the Kinesin-6 family member Kif20b disrupts normal cytokinetic abscission to cause microcephaly in

38 mice (Dwyer et al., 2011; Janisch et al., 2013; Little & Dwyer, 2019). The unique constraints of NSCs

39 during cell division have been hypothesized to make brain growth more vulnerable to defects in mitosis or

40 cytokinesis than other tissues. However, the cellular and developmental mechanisms that drive these

41 tissue-specific requirements are just beginning to be identified.

42   Cytokinesis has long been studied in cell lines and invertebrate organisms; this work has

43 identified many required proteins, and generated a model for the mechanism of abscission (Green et al.,

44 2012; Mierzwa & Gerlich, 2014). Beginning in anaphase following chromosome segregation, the

45 ingressing furrow compacts the central spindle microtubules and associated proteins into a structure

46 called the midbody, within the intercellular bridge. The midbody has a thick central bulge flanked on

47 either side by dense microtubule bundles. This complex structure consists of over 450 proteins that

48 mediate midbody formation, maturation, and the final scission event, in which the midbody flanks are

49 severed to separate the two daughter cells (Addi et al., 2020; Hu et al., 2012; Skop et al., 2004). The

50 abscission process involves both microtubule disassembly and membrane severing, thought to be

51 mediated by the endosomal sorting complexes required for transport (ESCRT) filaments (Connell et al.,

52 2009; Guizetti et al., 2011). The duration of abscission can be regulated, and slower abscission has been

53 linked to stemness (Chaigne et al., 2019; Lenhart & DiNardo, 2015; McNeely & Dwyer, 2020). After

54 abscission, the central bulge domain remains intact as the midbody remnant (MBR). Studies in

55 mammalian cell lines suggest that the MBR may mediate cell signaling and fate, either by binding cell

56 surface receptors or through uptake into daughter or neighbor cells (Crowell et al., 2014; Peterman et al.,

57 2019). We previously showed that in embryonic brains, MBRs can be visualized on the apical membranes

58 of cortical NSCs. Interestingly, MBRs are more persistent at early proliferative stages, and downregulated

59 later (McNeely & Dwyer, 2020).

60   The coiled-coil scaffolding protein Cep55 is thought to be essential for abscission in cell lines

61 (Fabbro et al., 2005; Zhao et al., 2006), with the key role of initiating the cascade of ESCRT recruitment

62 in midbodies (Stoten & Carlton, 2018). However, invertebrates lack a *Cep55* orthologue in their genomes,

63 yet complete abscission. Human mutations of *Cep55* cause a variety of brain malformations (Barrie et al.,

64 2020; Bondeson et al., 2017; Frosk et al., 2017; Rawlins et al., 2019). That human embryos with Cep55

65 mutation are able to develop at all is surprising, given that knockdown of Cep55 in human cell lines

66 caused almost universal failure of cell division (Fabbro et al., 2005; Zhao et al., 2006).

67   Here, we use a mouse knockout to elucidate the roles and requirements of Cep55 in abscission of

68 neural stem cells during brain development. We find *Cep55* is not absolutely required for abscission in

69 NSCs or other embryonic cells, but its loss causes abnormalities and increases failures. NSCs are

70 especially vulnerable to loss of Cep55 compared to other tissues, and brain size is disproportionally

71   reduced. Surprisingly, we find ESCRT recruitment is not eliminated in *Cep55 -/-* cell midbodies, though

72   it is impaired. We use fixed and live imaging of intact cortical epithelium to probe Cep55's role in

73   abscission. Additionally, we find the severe effect on the nervous system compared to other tissues

74   appears to be due to a specific p53 response triggering apoptosis, and test this using double knockout of

75   Cep55 and p53. This work underlines that studying cytokinetic proteins and processes in the context of

76   developing tissues is necessary to complement single cell models, in order to understand both the cellular

77   roles of specific proteins, and how their loss can cause various phenotypes at the tissue and organism

78   level.

79

80   **Results**

81

82   ***Cep55* knockout results in microcephaly with thin neuronal and axonal layers**

83

84   The mutation of *Cep55* used in this analysis is a 600 base-pair deletion encompassing all of exon

85   6 and flanking intronic sequence, generated by the CMMR (see Methods). The total murine *Cep55* gene

86   consists of 9 exons encoding a protein of 462 amino acids (AA) **(Figure 1A).** Cep55 protein domains

87   include two coiled-coil regions (CC1 and CC2) surrounding the ESCRT- and Alix- binding region

88   (EABR), and two ubiquitin binding domains (UBD) in the C-terminus (Lee et al., 2008; Morita et al.,

89   2007; Said Halidi et al., 2019). This deletion is predicted to result in a frameshift starting at AA 227,

90   resulting in multiple premature stop codons starting after AA 237. The Cep55 protein is undetectable by

91   immunoblot of homozygous mutant tissue lysates **(Figure 1B).**

92   Given that Cep55 was reported to be essential for mammalian cell division (Fabbro et al. 2005;

93   Zhao et al. 2006), we were surprised to discover that *Cep55 -/-* mice are born alive at expected Mendelian

94   ratios, and appear grossly normal with a slightly small body **(Figure 1C)**. However, while the pups

95   survive postnatally, they fail to thrive and die before or around weaning **(Figure 1 – figure supplement**

96   **1A-C)**. Upon inspection, *Cep55 -/-* pups have slightly flattened heads **(Figure 1C, arrow; Figure 1 –**

97   **figure supplement 1D),** and a 10% reduction in body length **(Figure 1D)**. Removing the brains from the

98   heads revealed that *Cep55 -/-* mice have severe microcephaly, with a 50% reduction in cortical area and

99   30% reduction in cortical length on postnatal day 0 (P0) **(Figure 1 E, G, H)**. Dissection of prenatal brains

100   showed a similar reduction in brain size compared to controls at embryonic day (E)14.5 and a smaller

101   (8%) reduction at age E12.5 **(Figure 1F-H)**. Cortical size is disproportionately reduced compared to body

102   size **(Figure 1I)**. However, eye size is normal in *Cep55 -/-* pups **(Figure 1 – figure supplement 1D-F)**. In

103   addition to reduced brain size, *Cep55 -/-* mice have reduced cortical thickness at P0 **(Figure 1J, K).** Thus,
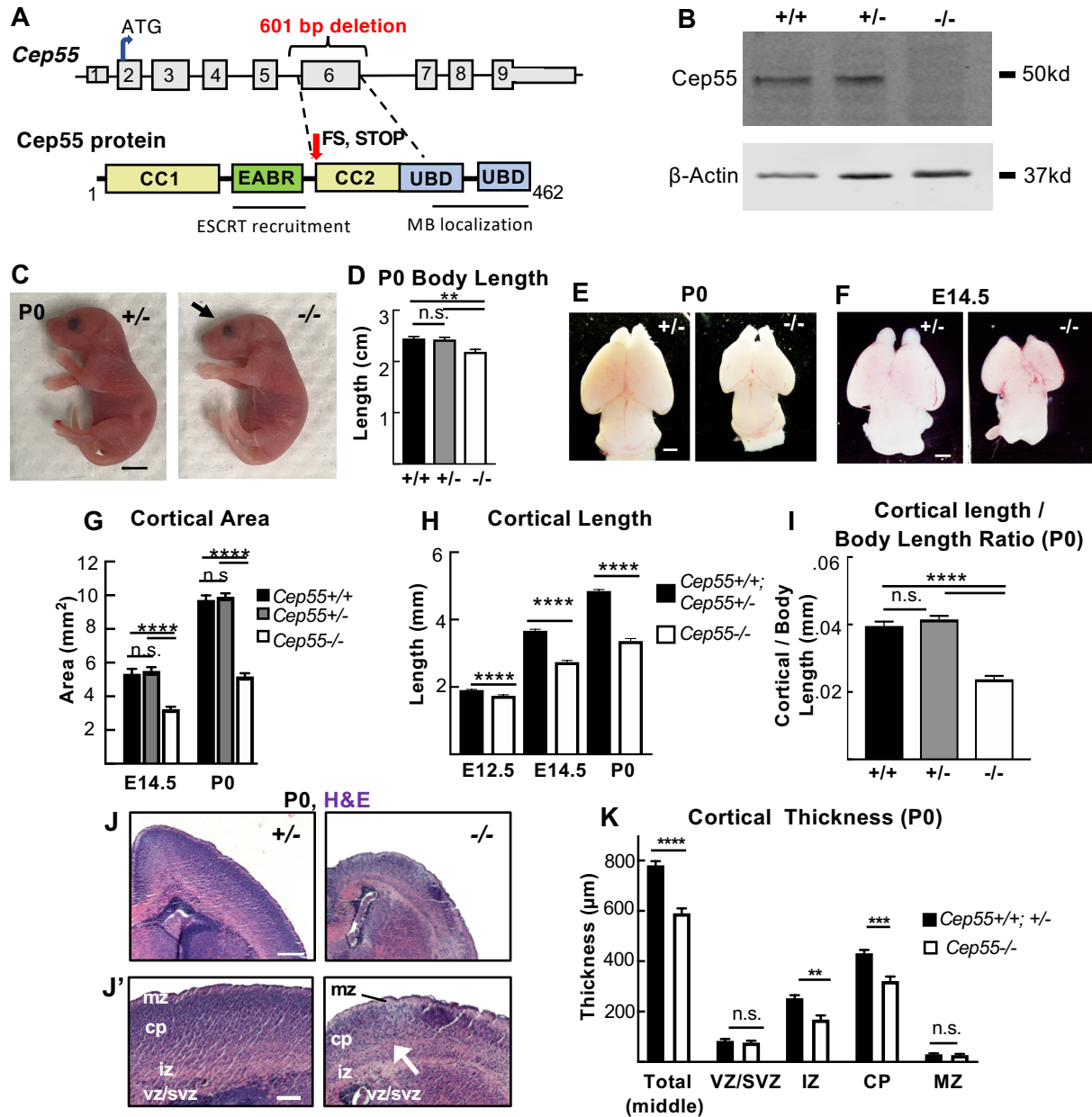
Figure 1: *Cep55* knockout causes microcephaly with severe thinning of neuronal and axon layers.

(A) Schematics of *Cep55* mouse gene and protein (not to scale). The 601 base-pair deletion includes all of exon 6 (311 bp) and portions of flanking introns. Cep55 protein domains include two coiled-coil regions (CC1 and CC2) surrounding the ESCRT- and Alix- binding region (EABR), and two ubiquitin binding domains (UBD). The deletion of exon 6 is predicted to result in a frameshift (FS) at amino acid 226 which causes multiple premature stop codons starting 12 residues later. **(B)** Immunoblots of E14.5 mouse embryonic fibroblast (MEF) lysates show the expected Cep55 protein product at approximately 55 kDa in wild-type and heterozygote samples, but not in ko samples. **(C,D)** Newborn *Cep55-/-* pups have 10% shorter body length and a flatter head (arrow) but otherwise appear morphologically similar to controls. **(E-G)** Representative images and measurements show mean cortical area is reduced in *Cep55-/-* brains at P0 and E14.5 compared to +/+ and +/- controls. **(H)** Mean cortical length is significantly reduced in *Cep55-/-* at E12.5, E14.5, and P0. **(I)** The cortical length in *Cep55-/-* P0 pups is disproportionately small relative to body size. **(J)** Representative images of P0 *Cep55+/-* and *-/-* coronal sections at level of corpus callosum, stained with H&E. mz, marginal zone; cp, cortical plate; iz, intermediate zone; vz/svz, ventricular/subventricular zone. *Cep55-/-* have reduced cell density in neuronal layers (J', arrow). **(K)** Mean total cortical thickness is significantly reduced in *Cep55 -/-* brains at P0. The VZ/SVZ and MZ thickness are unaltered, but the intermediate zone (IZ) and cortical plate (CP) are significantly thinner. For P0, n = 7 *Cep55+/+,* 14 +/- and 8 -/- mice. For E14.5, n = 5 *Cep55+/+*, 13 +/- and 10 -/- mice; for E12.5, n = 17 Cep55+/+;+/- and 9 -/- mice. For (L), n = 3 *Cep55+/+*, 5 +/-, and 5 -/- mice. Scale bars: C: 5 mm; E and F: 1 mm; J, 250 μm, J' 100 μm. n.s., not significant. ** $p < 0.01$; *** $p < 0.001$, **** $p < 0.0001$. D,G, and I: One-way ANOVA; H, K: Student's t-test.
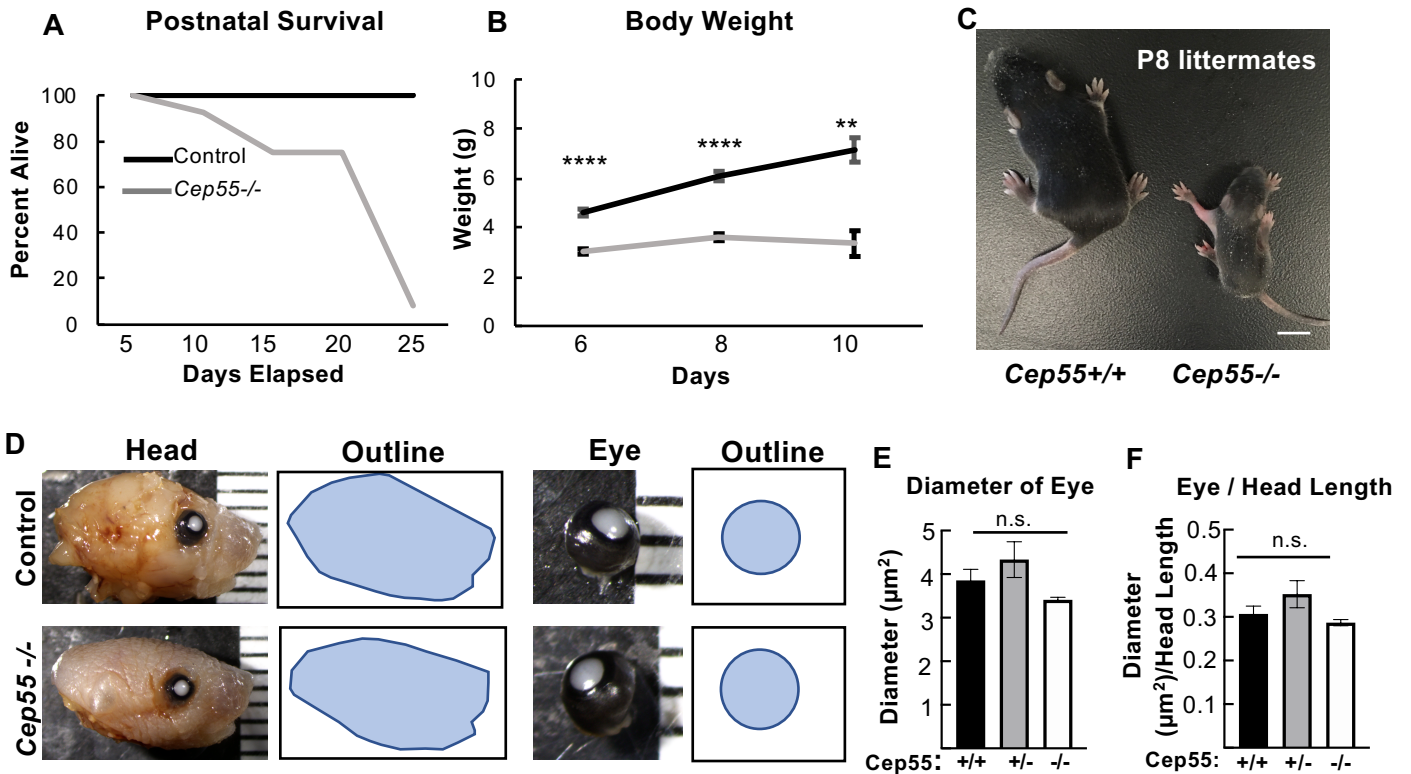
Figure 1 – figure supplement 1: *Cep55* knockout mice exhibit normal eye size and can survive postnatally, but exhibit failure to thrive and peri-weaning lethality.

(A-C) *Cep55 -/-* mice exhibit failure to thrive and pre-weaning lethality. (A) Most -/- pups die in the second or third week of life, and none survived past 25 days. n = 46 controls, 12 *Cep55-/-.* (B-C) *Cep55-/-* mice fail to gain weight between 6 and 10 days postnatally and are significantly smaller than controls. n, days: 6 = 13 controls and 6 -/-; 8 = 26 controls and 13 -/-, 10 = 11 controls and 4 -/-. **(D)** Examples of postnatal day 1 control and *Cep55 -/-* heads and dissected eyes. Note flatter head shape of *Cep55 -/-* apparent in the outline. **(E)** Average eye diameter is not significantly changed in *Cep55 -/-* pups. **(F)** Normalizing eye diameter to length of head showed no change between control and *Cep55 -/-*. n= 6 +/+, 9 +/-, 5 -/- pups. Scale bar: C, 5 mm. n.s., not significant, ** $p < 0.01$, **** $p < 0.0001$. B: Student's t-test, E, F: One-way ANOVA.

104 *Cep55* loss in mice appears to more drastically disrupt brain development than body development, and the

105 reduction in cortical growth correlates with the onset of neurogenesis around E12.5.

106   To determine if *Cep55* -/- mice have normal brain structure, we analyzed P0 cross sections

107 stained with hematoxylin and eosin (H&E) to label nuclei and axons, respectively. We noted a reduction

108 in size of all brain regions, including the forebrain, midbrain, and hindbrain **(Figure 1 – figure**

109 **supplement 2A)**. However, the forebrain appeared to be most severely affected. Interestingly, while

110 cortical thickness is reduced globally, the caudal cortex is the most severely affected **(Figure 1 – figure**

111 **supplement 2B, C)**.

112   To begin to determine the cellular cause of the thinner cortex in *Cep55* knockouts, we compared

113 the thicknesses of individual cortical layers in P0 control and mutant brains. Cortical stem (NSC) and

114 progenitor cells reside in the ventricular zone (vz) and subventricular zone (svz), while post-mitotic

115 neurons reside in the cortical plate (cp), and project their axons in the intermediate zone (iz). The cp and

116 iz of *Cep55* -/- cortices are significantly reduced in thickness, while the vz and svz are not **(Figure 1J, K)**,

117 suggesting a deficit of neurons. To examine the neuronal layers within the cortical plate, we labeled

118 control and *Cep55* -/- cortical sections with Ctip2, for layers 5 and 6, and Satb2, for layers 2-4 **(Figure 1**

119 **– figure supplement 2D)**. *Cep55* -/- cortical layers are ordered similarly to controls, but all are reduced in

120 thickness **(Figure 1 – figure supplement 2E)**. As a proportion of the total cp, the deep layers 5-6 of

121 *Cep55* -/- brains occupy more space, while the upper layers 2-4 occupy less **(Figure 1 – figure**

122 **supplement 2F)**. Interestingly, both the absolute number and the density of nuclei in layer 6 are

123 significantly reduced **(Figure 1 – figure supplement 2G, H)**. Together these data show the reduced

124 thickness of *Cep55* -/- cortices at birth is attributable to reduced thickness of all neuronal layers and

125 reduced number of neurons.

126

127 **NSCs are reduced and cortical layers are disorganized in *Cep55* knockout brains**

128

129   To begin to address the developmental defects leading to smaller brain size at birth, we examined

130 earlier stages of cortical development. Because *Cep55* -/- brains are already dramatically reduced in size

131 at E14.5, and this is an age when the cortical plate is forming, we analyzed numbers and positions of

132 NSCs, basal progenitors (BPs), and neurons at this age. By labeling E14.5 sections with neuronal tubulin

133 (Tubb3), we noted the cp was already thinner in *Cep55* -/- cortices, and the iz layer of axons was not

134 distinct **(Figure 2A)**. *Cep55* -/- cortical thickness is reduced by 12% at E14.5 (compared to 25% at P0,

135 **Figure 1K**), and similar to newborn brains, this reduction is due to thinner neuronal (cp and iz) rather

136 than proliferative layers (vz and svz) **(Figure 2B).** As a proportion of total thickness, the proliferative
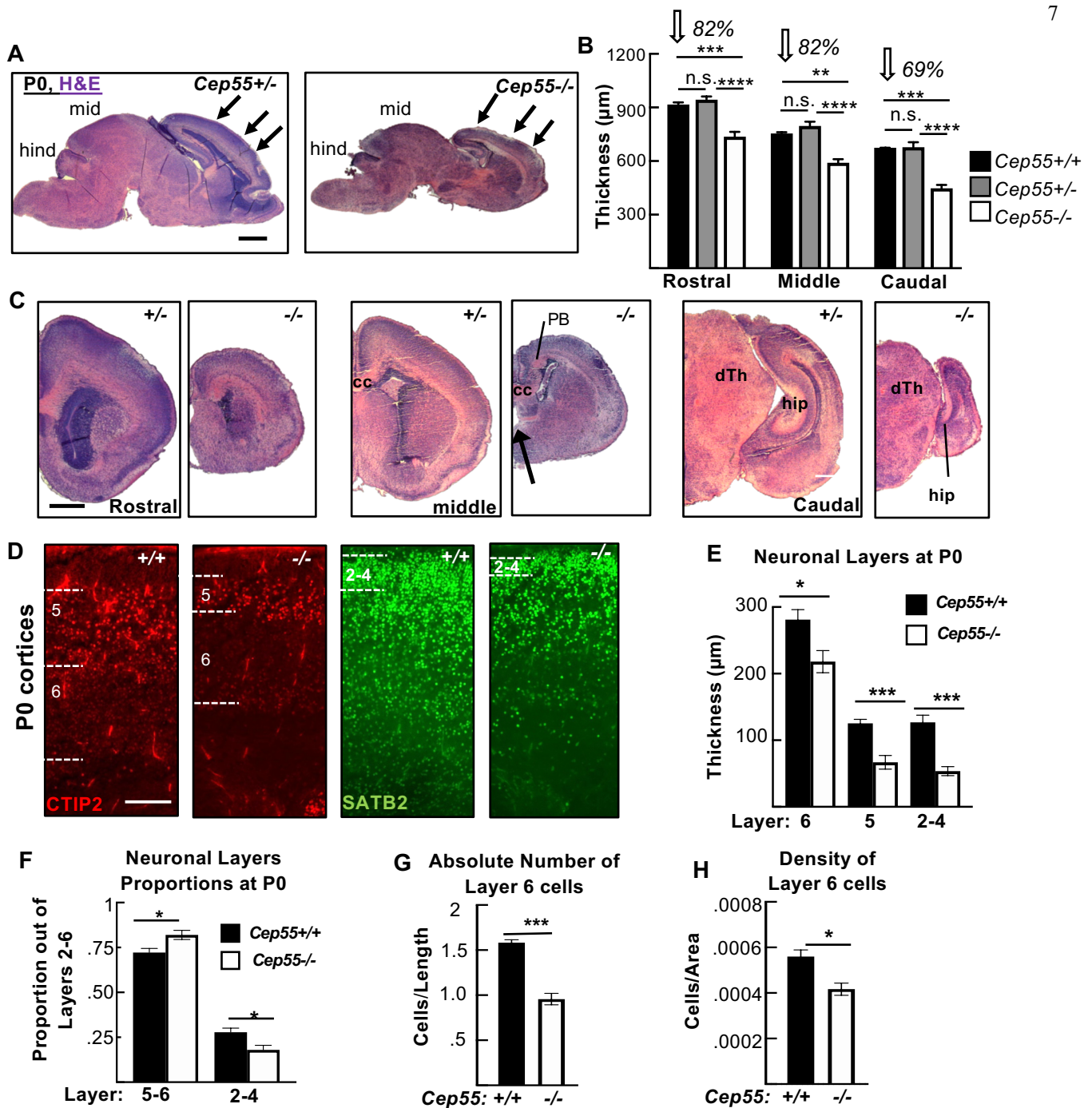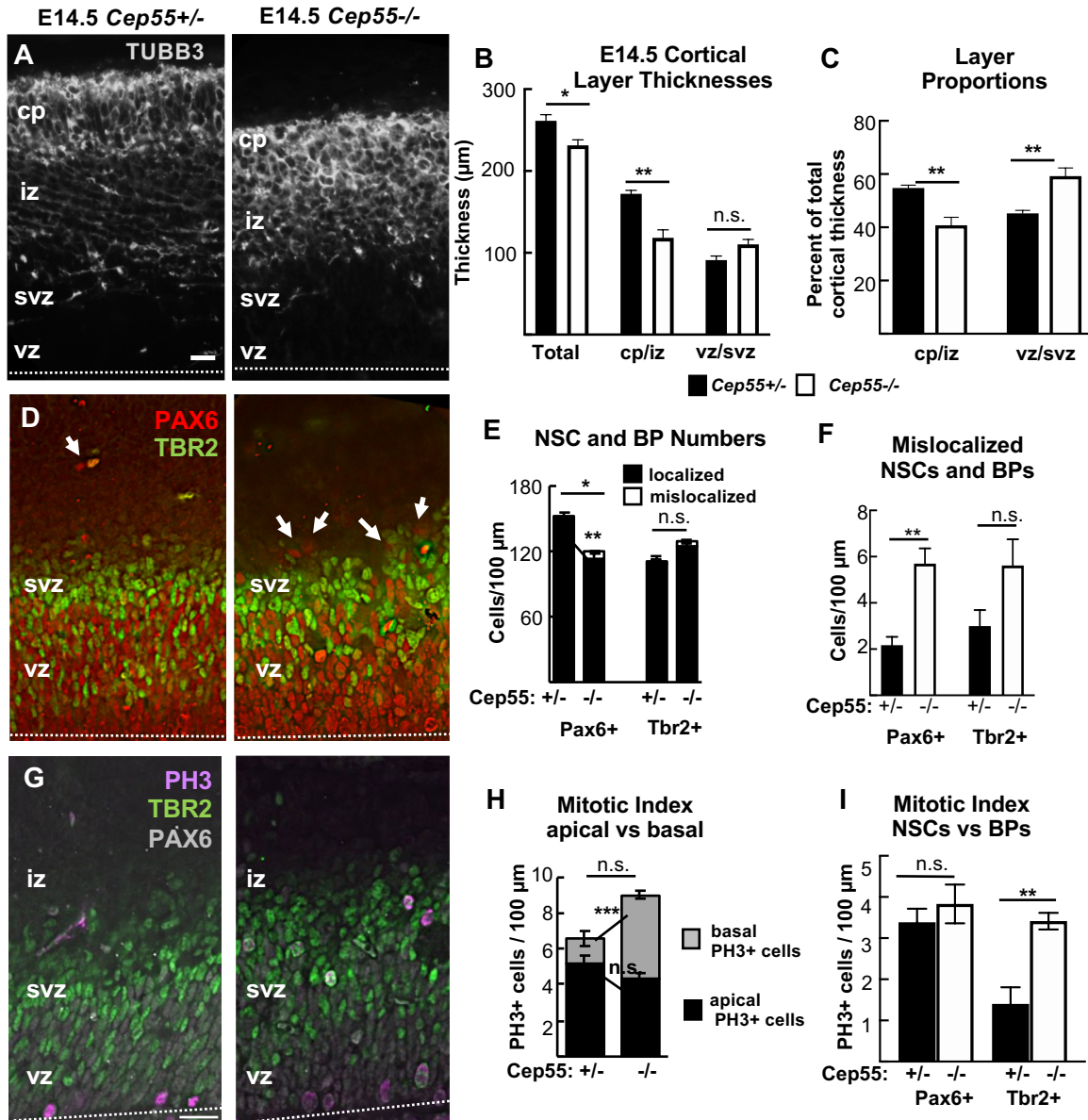
Figure 1 – figure supplement 2: *Cep55* knockout cortices are thinner, especially in caudal cortex, with reduced thickness but preserved order of neuronal layers and reduced neuron density.

(A, C) Representative *Cep55+/-* and *-/-* sagittal (A) and coronal (C) sections pf P0 brains stained with hematoxylin and eosin (H&E). Arrows in A mark approximate locations of rostral, middle ,and caudal, coronal sections in C. mid and hind signify midbrain and hindbrain; PB, Probst bundles of axons; hip, hippocampus; cc, corpus callosum; dTh, dorsal Thalamus. **(B)** The mean cortical thickness in *Cep55-/-* brains is 82% of normal in rostral and middle sections, and only 69% of normal in caudal sections. For B, n = 3 Cep55+/+, 5 Cep55+/-, and 5 Cep55-/- mice. **(D)** Representative images of P0 *Cep55+/+* and *-/-* cortical sections labeled with antibodies to Ctip2, marking layers 6 (faint staining) and 5 (bright staining) and Satb2, marking layers 2-4. **(E)** All neuronal layers are significantly thinner in *Cep55 -/-* cortices at P0 **(F)** Layers 5-6 occupy a larger proportion of cp while layers 2-4 occupy a decreased proportion of the cp in *Cep55-/-* cortices compared to +/+ controls. **(G)** The absolute number of layer 6 cells (# nuclei/length of cortex) is reduced by 40% in *Cep55-/-* cortices. **(H)** *Cep55-/-* layer 6 neurons are 25% less dense than wild-type cells (# nuclei/area). For G,H: n= 5 *Cep55+/+* and *4 Cep55-/-* mice; for I,K,J, n= 3 *Cep55+/+* and 3 *Cep55-/-* mice. Scale bar: A, C: 500µm, D: 100 µm. * p < 0.05; **p<0.01, ***, p<0.001, **** p < 0.0001. B: one-way ANOVA. G-J: t-test.

Figure 2: *Cep55* knockout cortex at E14.5 shows reduced and disorganized neuron and NSC layers.
(A) Representative images of cortical sections from *Cep55* +/- and -/- E14.5 embryos immunostained for neuron marker Tubb3 (gray) show cortical plate (cp) and axons in the intermediate zone (iz). In -/- images, the cp is disorganized the border between cp and iz is unclear. **(B)** Mean thicknesses of total cortex and neuron layer are significantly decreased in -/- brains. **(C)** The -/- cp/iz occupies proportionally less of cortical width than normal, while the vz/svz occupies more. **(D)** Cortical sections stained for NSC marker Pax6 (red) and basal progenitor (BP) marker Tbr2 (green) show NSCs in the vz of *Cep55-/-* brains are more disorganized, with some empty spaces (square), and some nuclei mislocalized basally above the svz (arrows). **(E-F)** NSCs (Pax6+) per cortical length are reduced in *Cep55-/-* and some mislocalized. BP numbers (Tbr2+) are not significantly changed. For B, total thickness, n = 7 +/- and 8 -/- brains. For B, cp/iz and vz/svz thickness, and for C,E,F, n= 4 +/- and 4 -/- brains. **(G)** Phospho-histone H3 (PH3) immunostaining is used to mark cells in mitosis. **(H)** *Cep55-/-* cortices show a normal number of mitotic cells (PH3+, magenta) at the apical membrane but an increased number of mitotic cells basally. **(I)** The mitotic index of NSCs (Pax6+) is normal, but of BPs (Tbr2+) is significantly increased in *Cep55 -/-* cortices. Dashed line in A,D,G = apical membrane. For H,I: n= 4 *Cep55+/-* and 4 -/- brains. Scale bar: (A,G): 20 µm. n.s.; not significant, * $p < 0.05$; ** $p < 0.01$; *** $p < 0.001$. All experiments, Student's t-test.

137   layer is increased **(Figure 2C)**. These data show that neuron production is already compromised before

138   E14.5.

139   The neurons of the cp are daughters of cell divisions of NSCs and basal progenitors**.** NSCs divide

140   many times, first symmetrically to multiply the NSCs, and then asymmetrically to produce BPs and

141   neurons. BPs divide symmetrically to produce two neurons. Neuron daughters exit the cell cycle and

142   differentiate. To determine whether the organization and numbers of NSCs and BPs in *Cep55* -/- cortices

143   are altered, we used Pax6 and Tbr2 antibodies to mark them respectively **(Figure 2D)**. We observe a

144   decrease in the number of NSCs in *Cep55* -/- cortices*,* while the number of basal progenitors is normal

145   **(Figure 2E)**. Notably, NSC and BP positioning appears disorganized, with a small but significant number

146   of NSC nuclei mislocalized at positions basal to the svz **(Figure 2D – arrows; Figure 2E, F)**.

147   Cep55 is not thought to have a primary role in mitosis (Fabbro et al., 2005). To check this, we

148   measured mitotic index in knockout brains, using phospho-histone3 (PH3) **(Figure 2G)**. There appears to

149   be a trend for increased numbers of mitotic cells in *Cep55* -/- cortical sections (6.69 versus 9 cells per 100

150   µm; p = 0.11) (**Figure 2H**); however, the increase is in basally rather than apically positioned mitotic

151   nuclei, and is due to an increase in the mitotic index of BPs, not NSCs **(Figure 2I)**. This suggests there is

152   not a primary defect in mitosis duration in *Cep55* -/- NSCs. Overall, these data demonstrate there are

153   reduced numbers of both NSCs and neurons in the *Cep55* -/- cortex, with slight disorganization of

154   layering, but not a significant increase in mitotic NSCs.

155

156   **Cep55 is expressed in proliferative cells in the brain and body, and is specifically detected in**

157   **midbodies during late abscission**

158

159   Having found defects in *Cep55* -/- neurons, NSCs and BPs, we needed to ascertain in which of

160   these cell types Cep55 is expressed. Previous RNA sequencing experiments found *Cep55* mRNA

161   expressed in proliferating cell types in early mouse embryos (Gao et al., 2017); and in the murine cerebral

162   cortex at E14.5 and P0 (Loo et al., 2019). RNA *in situ* hybridization shows *Cep55* is expressed in

163   proliferative zones of the cortex and eye at E14.5, but is not detectable in neuronal layers. Lower

164   expression in other proliferating tissues is observed **(Figure 3 – figure supplement 1A-C)**. We tested for

165   endogenous Cep55 protein expression and subcellular localization by immunohistochemistry on control

166   and knockout cells, and detected Cep55 protein in dividing NSCs of control embryos, but not knockouts

167   **(Figure 3A-C)**. Interestingly, Cep55 is specifically detected only at late stages of abscission: in late

168   midbodies as a disk at the center of the midbody, and in the post-abscission midbody remnants (MBRs).

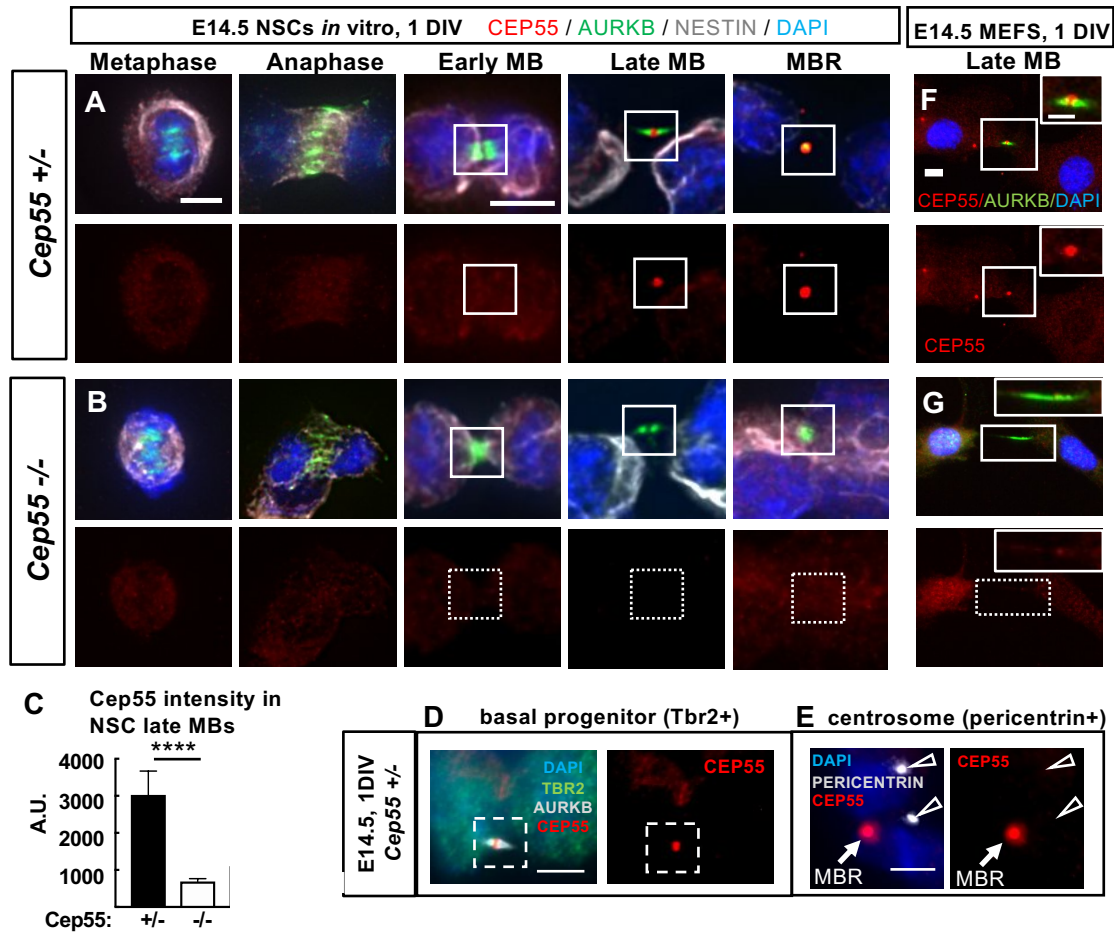169   No specific Cep55 signal was detected in metaphase, anaphase, or early midbodies. In basal progenitors

Figure 3: Cep55 protein localizes in late-stage midbodies of NSCs, basal progenitors and MEFs.
(A, B) Representative images of control (+/-) and *Cep55* knockout (-/-) E14.5 neural stem cells (NSCs) undergoing cytokinesis that were cultured for 1 day in vitro (DIV) fixed and immunostained for endogenous Cep55 (red), Aurora kinase B (green), Nestin for NSCs (grey) and DAPI. Cep55 is not detectable in mitotic spindles or centrosomes in metaphase, anaphase, or early midbody stage NSCs, but does accumulate in a disk in the center of late midbodies and in midbody remnants in control (A) but is undetectable in knockout (B) NSCs. **(C)** Quantification of endogenous Cep55 IF signal intensity in control and -/- NSCs midbodies. **(D)** Cep55 in a late-stage midbody of a basal progenitor from control brain. **(E)** Cep55 signal was not detected at centrosomes, marked by pericentrin, in NSCs (open arrows), but is detected in a nearby midbody remnant (closed arrow). **(F, G)** *Cep55+/+* MEFs show a similar pattern of Cep55 localization as NSCs, with accumulation only in late-stage midbodies (F), but is undetectable in *Cep55-/-* MEF midbodies (G). Scale bars: A, metaphase and early midbody: 5 μm; D: 4 μm; E: 5 μm; F: 10 μm, inset 5 μm. ****, p <0.0001, Student's t-test.
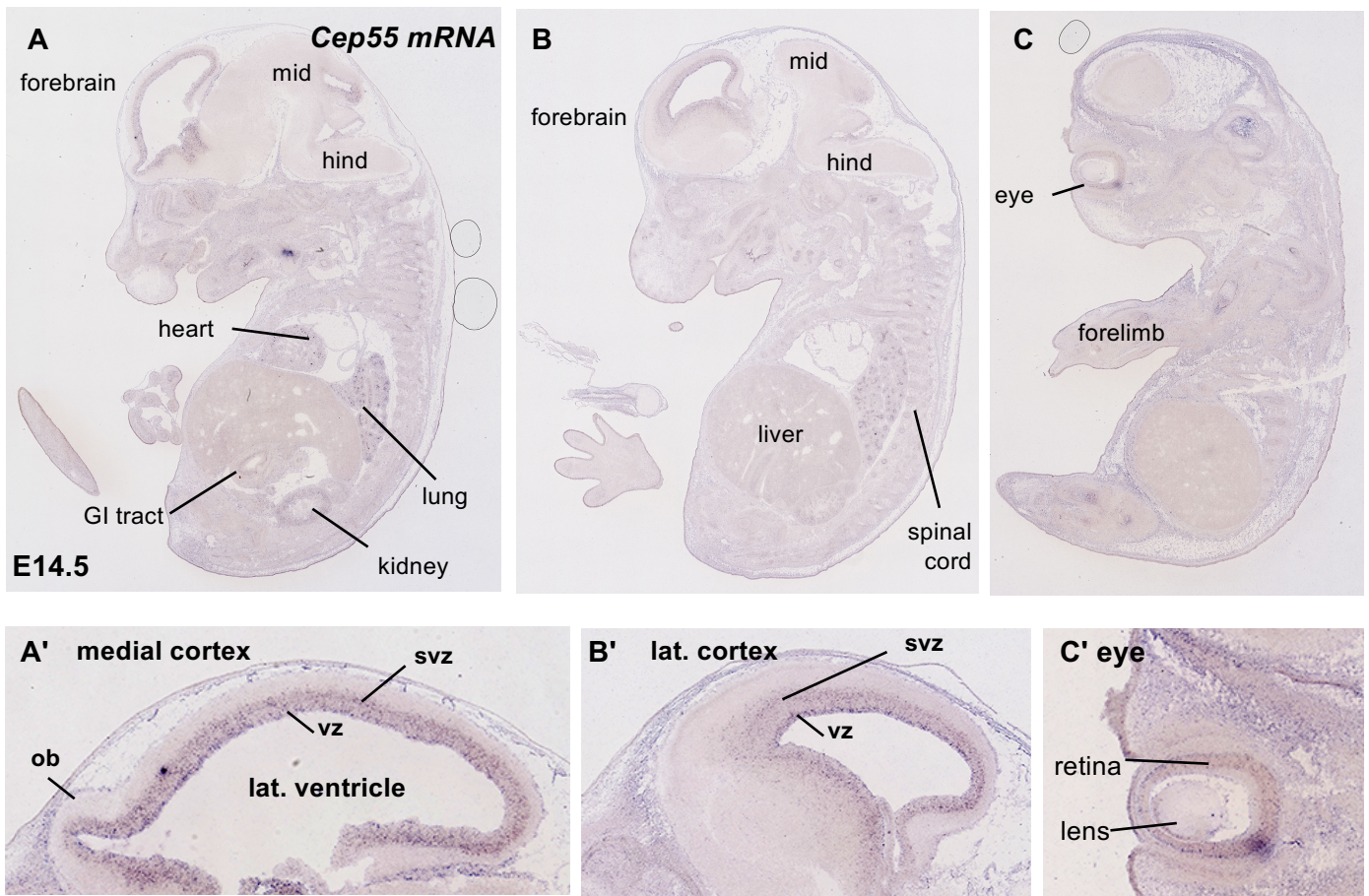
Figure 3 – figure supplement 1: *Cep55* **mRNA is expressed in proliferating embryonic tissues, including germinal zones of the nervous system.**

(A-C) Images of RNA in situ hybridization for *Cep55* mRNA on sagittal sections of E14.5 mouse embryos. *Cep55* is expressed in germinal zones of the nervous system including brain and eye, as well as widespread in proliferating embryonic tissues. Structures of interest in sagittal sections are labeled in whole embryo (A-C) and in zoomed forebrain (A'-B') and eye (C') images. mid: midbrain; hind: hindbrain; ob: olfactory bulb; vz: ventricular zone; svz: subventricular zone; lat vent: lateral ventricle . (Images from GenePaint, https://gp3.mpg.de, Visel et al. 2004).

170   from control brains, Cep55 has the same localization pattern **(Figure 3D)**. We do not detect Cep55

171   protein at centrosomes **(Figure 3E)**, concurring with others (Bastos & Barr, 2010; Zhao et al., 2006).

172   To investigate whether Cep55 is expressed in cells of non-neural tissues, we dissociated mouse

173   embryonic fibroblasts (MEFs) from E14.5 control and *Cep55* -/- embryo bodies. We noted the same

174   expression pattern in MEFs as in NSCs, with detectable signal above background only in late-stage

175   midbodies of control MEFs **(Figure 3F, G)**. Thus, we find Cep55 is expressed in multiple proliferating

176   embryonic cell types – NSCs, BPs and MEFs – and that it accumulates specifically at the late stage of

177   abscission in the central bulge of the midbody.

178

179   **Midbody defects in fixed cortices of *Cep55* knockouts are consistent with delays in NSC abscission.**

180

181   Based on the specific localization of Cep55 to late-stage NSC midbodies, as well as the prior

182   reports of a requirement for Cep55 in completion of abscission in cell lines, we hypothesized that

183   microcephaly in *Cep55* -/- mice is due to a primary defect in abscission completion. However, the growth

184   of the brain (albeit less than normal), and almost normal body size of *Cep55* knockouts suggest that

185   abscission is completing in most cells. To begin to address whether abscission processes in *Cep55* -/-

186   brains are normal, we used a fixed cortical slab preparation in which we can image and quantitatively

187   analyze many NSCs undergoing mitosis and cytokinesis at the ventricular surface **(Figure 4A-B)** (Janisch

188   & Dwyer, 2016; Janisch et al., 2013). By labeling the NSC apical cell junctions with ZO-1, we observe

189   that *Cep55* -/- endfeet are more variable in size, with many abnormally large endfeet (**Figure 4C**). Indeed,

190   quantification shows a striking decrease in the density of apical endfeet **(Figure 4D)**. Since the apical

191   membrane expands during mitosis, we quantified the apical mitotic index of NSCs, using phospho-

192   histone H3 (PH3), but it is not altered in *Cep55* -/- cortices **(Figure 4C - left panels, E)**, consistent with

193   our finding in cross sections **(Figure 2H)**. However, the midbody index, the percent of NSCs in

194   abscission, is increased by approximately 25% at E14.5 **(Figure 4C - right panels, F)**. These data

195   suggest that in *Cep55* knockout cortices, NSCs may take longer to complete abscission. As the abscission

196   process proceeds, midbodies mature by becoming thinner, and then forming constriction sites on each

197   flank, where microtubule disassembly and membrane scission occurs (Guizetti et al., 2011). We observe

198   fewer midbodies with constriction sites in *Cep55* -/- brains **(Figure 4G),** and more short midbodies

199   **(Figure 4H).** There was no significant difference in midbody widths (data not shown). These data suggest

200   that without Cep55, midbodies are able to compact their microtubules to become thinner as they mature,

201   but have a defect in making the constriction sites, and abscission duration is longer than normal.

202   Since Cep55 protein is abundant in midbody remnants (MBRs) **(Figure 3A)**, we investigated

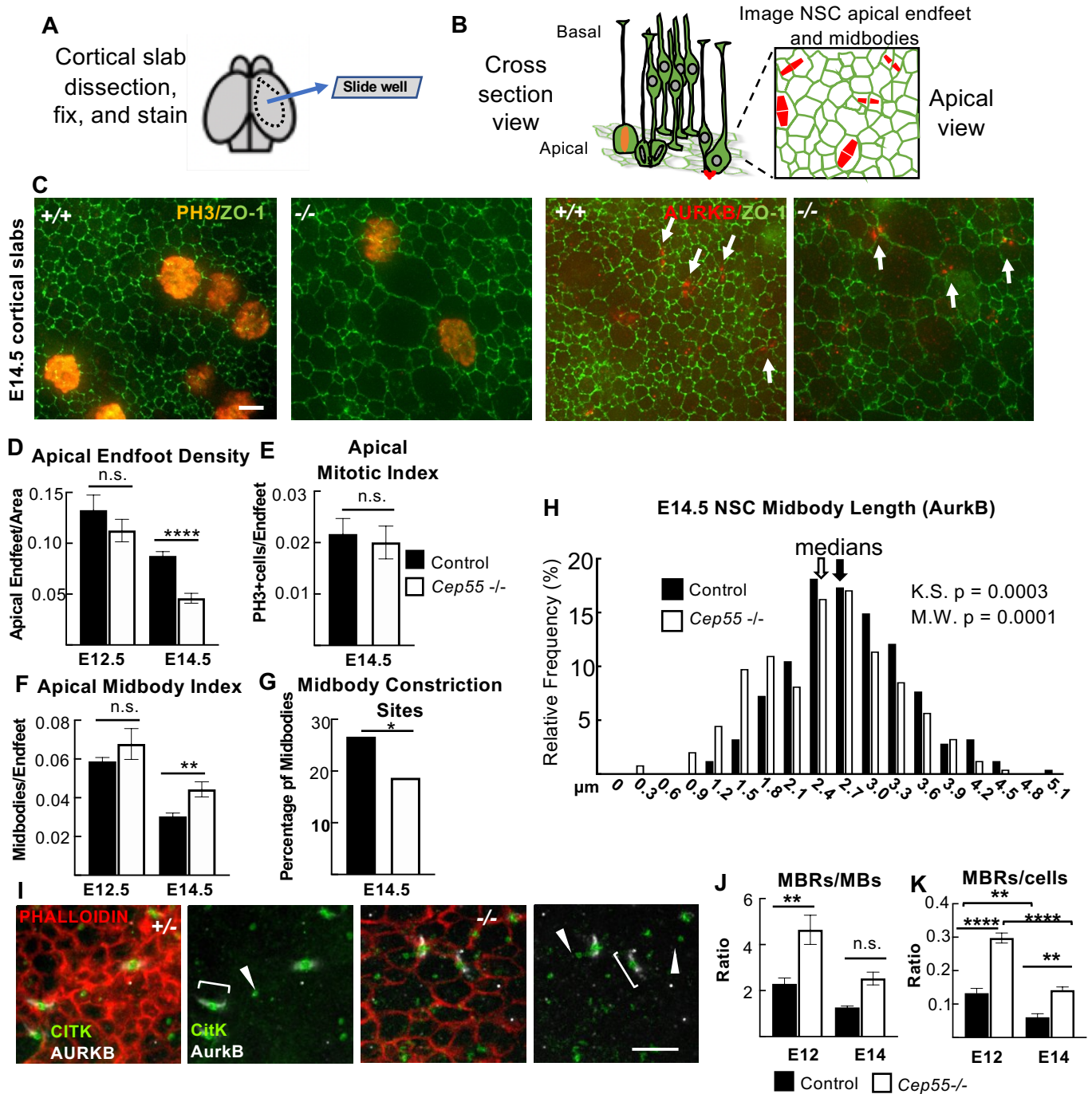203   whether Cep55 loss alters MBR numbers at the apical membranes of NSCs, using Citron kinase (CitK) as

Figure 4: *Cep55* knockouts display NSC midbody defects in cortical slab preparations.
(A, B) Schematics of cortical slab dissection, and cross section vs. apical membrane views of NSCs undergoing cytokinesis. **(C)** E14.5 cortical slabs immunostained for apical junctions (ZO-1, Zona-Occludens-1), and mitotic chromatin (PH3+) or midbodies (AURKB, Aurora B kinase). **(D)** Mean apical endfoot density is reduced in *Cep55 -/-* at E14.5. For D, E12.5: N= 4 +/- slabs (4 brains), 4 -/- slabs (4 brains). E14.5: N = 8 control slabs (6+/+, 2+/- brains) and 7 -/- slabs (6 brains). **(E-F)** Mitotic index is normal, but midbody index is significantly increased at E14.5. For E, N= 6 control slabs (4+/+, 2+/- brains), 6 -/- slabs (5 brains). For F, E12.5: N= 4 +/- slabs (4 brains), 4 -/- slabs (4 brains). E14.5: N= 6 control slabs (4 +/+, 2+/- brains), 5 -/- slabs (5 brains). **(G)** A smaller percentage of Cep55 -/- midbodies have visible constriction sites. **(H)** Cep55 -/- midbodies tend to be shorter than controls (measured by AurkB immunolabeling). Medians: 2.7 μm for +/+, 2.5 μm for -/-. Bin = 0.3μm. For G, H, N= 353 control midbodies (5+/+, 2+/- brains), 246 -/- midbodies (5 brains) **(I)** E14.5 slabs immunostained for AurkB to mark pre-abscission midbody flanks (brackets), and citron kinase (CitK) to mark midbody bulges and post-abscission MBRs (arrowheads). **(J,K)** MBRs are increased in *Cep55-/-* brains, normalized to MB number or NSC (endfoot) number. For J,K, E12.5 and E14.5: N= 4 control slabs (2 +/+, 2+/- brains), 4 -/- slabs (4 brains). Scale bars: B: 2 μm I: 5μm. *p<0.05, **p<0.01, ***p<0.001, ****p<0.0001, n.s., not significant. D,F-G: Student's T-test, J,K: ANOVA, E: Fisher's exact test.

204   a marker (Ettinger et al., 2011; Gruneberg et al., 2006). Remarkably, there are approximately twice as

205   many MBRs present on the apical membranes of *Cep55 -/-* brains as in control brains, whether

206   normalized to midbody number or cell number **(Figure 4I-K)**. This could be another manifestation of

207   delayed abscission, at a late stage when the flanks are no longer detectable with Aurora B staining. It

208   could also represent a role of Cep55 in MBR disposal. Altogether, theses analyses in fixed brains show

209   midbody abnormalities that are consistent with delayed abscission of NSCs when Cep55 is absent.

210

211   **Cep55 knockout NSCs can complete microtubule disassembly, but it is delayed**

212

213   To directly test whether abscission is delayed or fails in NSCs of *Cep55 -/-* cortex, we performed

214   time-lapse imaging of abscission *in vivo*, in live cortical slab explants, using a method we developed

215   previously (McNeely & Dwyer, 2020)**.** By dissecting cortical slabs from embryonic brains of a

216   membrane-GFP mouse line, and incubating them with the cell-permeable far-red fluorescent microtubule

217   dye SiR-tubulin, we can image individual NSCs at the apical membrane undergoing cytokinesis from

218   furrowing to abscission. As the cleavage furrow ingresses towards the apical membrane, the midbody

219   forms as a tight bundle of microtubules, the central bulge becomes apparent, and then microtubule

220   disassembly occurs on each midbody flank independently **(Figure 5A)**. We previously showed that in

221   control E13.5 NSCs *in vivo*, abscission takes on average 50 minutes to complete, with a wide range of

222   times observed, and microtubule disassembly occurs on both sides of the midbody flank in the majority of

223   divisions (McNeely & Dwyer, 2020).

224   Using this method, we quantified several aspects of the abscission process in *Cep55 -/-* NSCs:

225   midbody formation, midbody structure, and time to abscission (ascertained as microtubule disassembly)

226   on one or both flanks. Unexpectedly, we find the vast majority (92%) of *Cep55 -/-* NSCs are able to

227   complete abscission. However, these knockout NSCs do have a significant increase in average time to the

228   first abscission (delay of 23 minutes, **Figure 5B**). They are also able to complete bilateral abscissions:

229   eighty percent of both control and *Cep55 -/-* NSCs have observable second abscissions on the other

230   midbody flank **(Figure 5C)**. But again, the time to the second abscission is significantly increased in

231   knockout NSCs **(Figure 5D)**. Cumulative frequency plots illustrate the slower abscission kinetics in the

232   *Cep55 -/-* NSCs **(Figure 5E-F)**.

233   We did observe a small number of *Cep55* knockout NSCs that displayed abnormalities at an

234   earlier step of cytokinesis. Notably, there is a significant increase in the number of *Cep55 -/-* NSCs that

235   have tripolar mitotic spindles (7%, 6 out of 81 knockout NSCs imaged versus 0 out of 71 in controls)

236   **(Figure 5G-H)**. Of these 6 NSCs with tripolar spindles, four progressed into tripolar midbodies, which

237   remarkably were still able to undergo microtubule disassembly, one regressed, and one drifted out of the
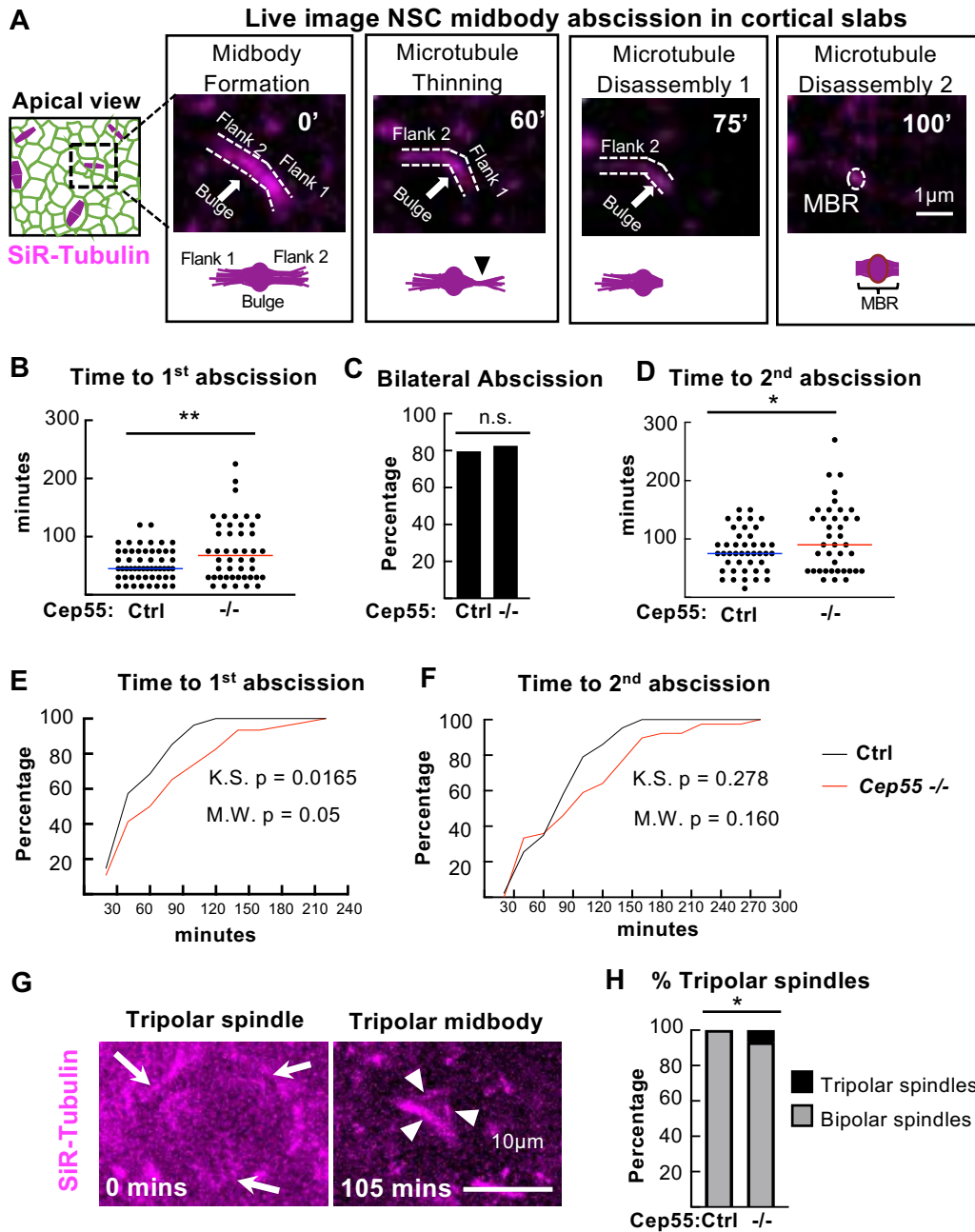
Figure 5: *Cep55* knockout causes delayed midbody microtubule disassembly during NSC abscission.
(A) Schematics and time-lapse images of an E13.5 NSC in a cortical slab explant undergoing midbody abscission. Microtubules are labeled by SiR-Tubulin. Distinct steps shown: midbody formation, flank 1 thinning, microtubule disassembly on flank 1 (1st abscission), and microtubule disassembly on flank 2 (2nd abscission). After bilateral flank disassembly, the midbody remnant (MBR) is left at the apical membrane. **(B-D)** Time from midbody formation to complete 1st abscission and 2nd abscission are increased in *Cep55-/-* NSCs, but there is no change in the percentage of bilateral abscissions detected. **(E, F)** Cumulative frequency plots for the 1st abscission and 2nd abscission show the curves are shifted to the right in -/- NSCs. **(G)** *Cep55-/-* NSC with a tripolar spindle (arrows point to spindle poles) proceeded to form a tripolar midbody at 105 minutes. (arrowheads point to midbody "flanks"). **(H)** Tripolar spindles are increased in *Cep55* -/- cortices. For B,C, E, N= 54 control cells (2 +/+, 1 +/- slabs), 46 -/- cells (4 slabs); D,F: N= 43 control cells,39 -/- cells. G: N= 71 control cells (2+/+, 1+/- slabs) and 86 -/- cells (4 slabs). *p<0.05, **p<0.01. B,D: T-test. E,F: K-S and M-W tests. C,H: Fisher's Exact test.

238   imaging field. We observed a few *Cep55 -/-* NSCs that had bipolar spindles that initiated a furrow but did

239   not complete (4/50, compared to 0/54 control NSCs). In three of these NSCs, the furrow only partly

240   ingressed then regressed, so the midbody never formed, while in the other, the midbody formed, but then

241   the membrane regressed. Taken together with our preceding data on Cep55 protein localization and fixed

242   midbody abnormalities, the findings indicate that the primary function of Cep55 in NSCs is to promote

243   timely abscission, with particular effects on the kinetics of late steps such as constriction site formation

244   and microtubule disassembly.

245

246   ***Cep55* knockout NSCs and MEFs have decreased but not eliminated ESCRT recruitment to late-**

247   **stage midbodies.**

248

249   Since *Cep55 -/-* NSCs have delayed abscission, and Cep55 is thought to recruit other abscission

250   proteins, we wanted to determine if other known abscission proteins were altered. The current model for

251   the mechanism of abscission, developed from mammalian cell lines and invertebrates, proposes that at the

252   late stage of abscission, endosomal sorting complexes required for transport (ESCRT) components are

253   recruited to the midbody, and then form helical filaments extending from the central bulge to constriction

254   sites, compacting microtubules and pulling the plasma membrane close enough for membrane scission

255   (Christ et al., 2017; Goliand et al., 2018; Guizetti et al., 2011; Stoten & Carlton, 2018). Cep55 is thought

256   to be necessary to recruit this abscission machinery to the midbody in human cells through interactions

257   with ESCRT-I/TSG101 and Alix. Then TSG101 and Alix both recruit ESCRT-III, which assemble into

258   filaments (Carlton et al., 2008; Christ et al., 2016; Lee et al., 2008; Morita et al., 2007) **(Figure 6A)**.

259   Notably, Cep55 is absent in invertebrate genomes, yet their midbodies still recruit ESCRTs to mediate

260   abscission. Therefore, we asked whether abscission in *Cep55 -/-* NSCs is accomplished with or without

261   the ESCRT machinery. First, we tested for the localization of endogenous Tsg101 and Alix in midbodies

262   of control and *Cep55 -/-* NSCs. Approximately one-third of control NSC midbodies have Alix or Tsg101

263   present at the midbody center, reflecting that recruitment is temporally regulated and occurs only at late

264   abscission stages. Among *Cep55 -/-* NSC midbodies, however, only about 5% had detectable Alix and

265   Tsg101 **(Figure 6B)**. This suggests that in the absence of Cep55, ESCRT component recruitment may be

266   delayed, or total protein recruitment may be decreased.

267   Next, we used MEFs to further analyze midbodies and ESCRT recruitment when Cep55 is absent,

268   since MEF cells and midbodies are much flatter than NSCs and easier to image. Control MEFs exhibit

269   identical Cep55 localization in late-stage midbodies as NSCs do **(Figure 3F)**. Additionally, an antibody

270   against the downstream ESCRT-III component, Chmp2a, works on MEFs **(Figure 6C)**. Cep55 was

271   previously suggested to be required for formation of the dense central midbody matrix in HeLa cells,

272 which appears as an unlabeled "dark zone" with alpha-tubulin or Aurora B antibody immunostaining

273 (Zhao et al., 2006). We tested this in MEFs, but the dark zones were equally detected in *Cep55* -/- MEFs

274 as controls **(Figure 6D)**. *Cep55* -/- MEF midbodies had similar length and width to controls (data not

275 shown). Next, we tested Alix and Tsg101 recruitment, and found similarly to NSCs, the percentages of

276 *Cep55* -/- MEF midbodies with detectable endogenous Alix and TSG101 are significantly decreased

277 compared to controls **(Figure 6C, E)**. There is also a trend for reduced midbodies with the ESCRT-III

278 component Chmp2a detectable **(Figure 6E)**. Interestingly, if we just consider midbodies that have formed

279 constriction sites, about 40% of control MEFs have ESCRT localization, versus 15% of the *Cep55* -/-

280 MEFs, suggesting that constriction sites can form before or independently of ESCRT recruitment **(Figure**

281 **6F).**

282 Next, we asked whether the minority of *Cep55* -/- MEF midbodies with detectable ESCRTs had

283 normal distribution of that ESCRT within the midbody. We evaluated ESCRT protein signal intensity

284 using line scans drawn lengthwise along the midbody. In controls, a peak of ESCRT intensity is seen as

285 expected in the central matrix/ "dark zone" between the Aurora B stained flanks **(Figure 6G-I, controls)**.

286 In *Cep55* -/- midbodies that had detectable Alix, the average peak intensity of Alix fluorescence is

287 significantly decreased, and the peak of intensity at the dark zone is lost **(Figure 6G)**. Surprisingly, for

288 Tsg101-containing *Cep55* -/- midbodies, there is not a decrease but a slight increase in peak intensity of

289 Tsg101, and the intensity pattern is similar to controls **(Figure 6H)**. We found a trend for decreased peak

290 Chmp2a fluorescence compared to controls **(Figure 6I)**. This suggests the interesting possibility that Alix

291 and Tsg101 recruitment are affected differently by loss of Cep55. Together these data indicate that Cep55

292 is not essential for ESCRT component recruitment to the midbody in NSCs and MEFs, but suggests that

293 Cep55 may increase or accelerate their recruitment to ensure efficient abscission.

294

295 ***Cep55* knockout mice have increased numbers of binucleate cortical cells and MEFs**

296

297 Our analyses of midbodies and abscission in NSCs of the *Cep55* knockout so far suggest that

298 most NSCs can complete abscission in the absence of *Cep55*, but that the process is slower and a subset

299 of cells may fail. To assay cytokinesis success and failure in a larger sample of cells, we analyzed DNA

300 content of embryonic cortical cells with flow cytometry. Dissociating cells of E15.5 cortices and labeling

301 DNA with propidium iodide, we found 30% of *Cep55* -/- cortical cells have 4N DNA content compared

302 to 2% in controls, a 15-fold increase **(Figure 7A)**. An increase in cells with 4N DNA content could come

303 from either an arrest in G2 /M phase, or failed cytokinesis resulting in formation of a binucleate or

304 tetraploid progenitor or neuron. Since we did not see significantly increased numbers of PH3+ cells in

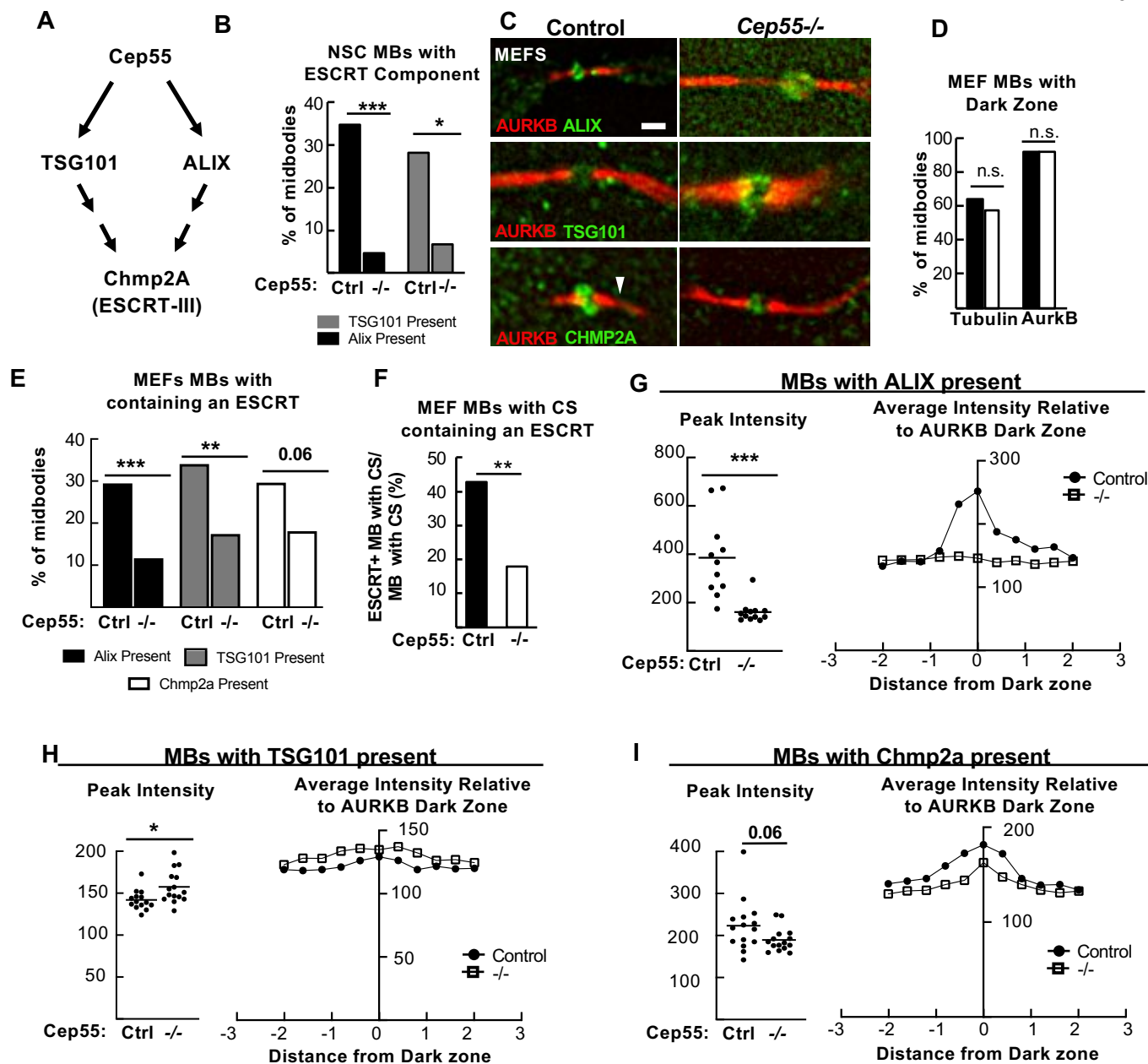305 *Cep55* -/- cortices **(Figure 2H)**, this suggests the presence of binucleate/tetraploid cells. To investigate

Figure 6: *Cep55* knockout NSCs and MEFs have reduced but not eliminated ESCRT recruitment to midbodies.
(A) Model from literature for Cep55 recruiting ESCRTs in midbodies (MBs). **(B)** *Cep55-/-* NSC midbodies are much less likely to have detectable Alix or TSG101. Alix: N= 49 NSC control MBs (3 animals, 3 coverslips); N= 46 -/- MBs (2 animals, 3 coverslips); TSG101: N= 32 control (2 animals, 2 coverslips), N= 45 -/- (3 animals, 3 coverslips). All E14.5 NSCs 1 DIV. **(C)** Representative images of MBs of Mouse embryonic fibroblasts (MEFs) cultured for 1 day, from control or *Cep55-/-* E14.5 embryos, immunostained for ALIX, TSG101, or Chmp2A. Arrowhead, constriction site. Scale Bar 1μm. **(D)** Central dark zones were detected at normal percentage in -/- MEF MBs, using alpha-tubulin or AurkB immunostaining. For D: N= 402 control, 355 -/- MBs (5 animals, 6 coverslips each). **(E)** *Cep55-/-* MEF midbodies are much less likely to have detectable Alix , TSG101, or Chmp2a than controls. Alix: N= 153 control, 129 -/- MBs (4 animals, 4 coverslips each); Tsg101: N= 141 control, 132 -/- MBs (4 animals, 4 coverslips each); Chmp2a: N= 108 control, 105 -/- MBs (3 animals, 3 coverslips each). **(F)** The percentage of MBs with constriction sites (CS) that contain detectable ESCRT is decreased in -/- MBs. N (midbodies with constriction sites) = 110 control, 95 -/-, (5 animals, 11 coverslips each). **(G-I)** MBs with ESCRT present were analyzed by fluorescence intensity linescans through the central dark zones. Alix peak is severely reduced in -/- MBs, but Tsg101 and Chmp2a peaks are not. Alix: N=11 control,-/- MBs (2 animals, 2 coverslips, 1 experiment); Tsg101: N=14 control, 15 -/-MBs (2 animals, 2 coverslips, 1 experiment); Chmp2a: N= 15 control, -/- MBs (2 animals, 2 coverslips, 1 experiment). * p < 0.05; ** p < 0.01; *** p < 0.001. C-G: Fisher's exact test; H-J,: Student's t-test.

306   whether cells with 4N DNA content were progenitors or neurons, we used Ki67 and DAPI co-labeling to

307   differentiate cycling progenitor cells (Ki67+) from non-cycling neurons (Ki67-) cells. Interestingly, we

308   observed an increased 4N DNA peak in both Ki67+ **(Figure 7B)** and Ki67- *Cep55* -/- cells **(Figure 7C)**.

309   In controls, there is no 4N DNA peak in Ki67-negative cells, because neurons are post-mitotic **(Figure**

310   **7C, left)**. These data suggest that in *Cep55* -/- cortices, there are significant numbers of binucleate

311   neurons and NSCs.

312   To further investigate whether there are binucleate NSCs and/or neuron populations in *Cep55* -/-

313   cortices, we imaged dissociated, cultured cortical cells from E14.5 cortices. We used Nestin

314   immunostaining to mark NSCs, and actin (phalloidin) and DAPI staining to differentiate cells with one or

315   two nuclei. Indeed, we observed increased percentages of binucleate cells in *Cep55* -/- cultures, including

316   approximately 24% of NSCs (Nestin+) and 12% of neurons (Nestin-) **(Figure 7D-F)**. These data show

317   that *Cep55* knockout results in significant numbers of binucleate NSCs and neurons in the brain.

318   Since the brain size is more severely affected than body size in *Cep55* knockouts **(Figure 1D)**,

319   We wondered whether binucleation is a consequence of *Cep55* loss in non-neural cell types too. Cep55 is

320   localized in embryonic fibroblast midbodies in a similar distribution as seen in NSCs **(Figure 3F)**, and its

321   loss causes decreased recruitment of ESCRTs **(Figure 6E)**. Indeed, we do observe a doubling of

322   binucleate cells in *Cep55* -/- MEF cultures compared to controls **(Figure 7G, H)**. Thus, while not as

323   dramatic as seen in NSC cultures, Cep55 loss does lead to binucleation in MEFs as well.

324

325   **Apoptotic cells are increased in *Cep55* knockout neural but not non-neural tissues during**

326   **embryogenesis**

327

328   Abscission defects and binucleation have been linked to apoptosis of NSCs and neurons in other

329   genetic mouse microcephaly mutants (Bianchi et al., 2017; Little & Dwyer, 2019; Moawia et al., 2017).

330   The disorganization and reduced cell numbers we noted in *Cep55* -/- cortices suggest some cells could be

331   dying. To assay for apoptosis, we labeled cortical sections with antibodies to cleaved-caspase 3 (CC3). In

332   control developing cortex, apoptotic cells are only rarely detected, but there is a striking increase in

333   apoptotic cells in *Cep55* -/- cortices **(Figure 8A)**. Apoptosis is most increased in the proliferative zones,

334   but is also increased in the cortical plate (cp , neuronal layer) **(Figure 8B)**. This suggests widespread

335   apoptosis in multiple cortical cell types, with the highest increase in dividing cell types, NSCs and BPs.

336   Since brain size is already significantly decreased at E14.5, we looked at an earlier age for apoptosis.

337   Indeed, apoptosis is dramatically increased in *Cep55* -/- cortical epithelium at E10.5, when the cortex

338   consists only of NSCs **(Figure 8C-D)**. Therefore, we conclude that apoptosis of primarily NSCs but also

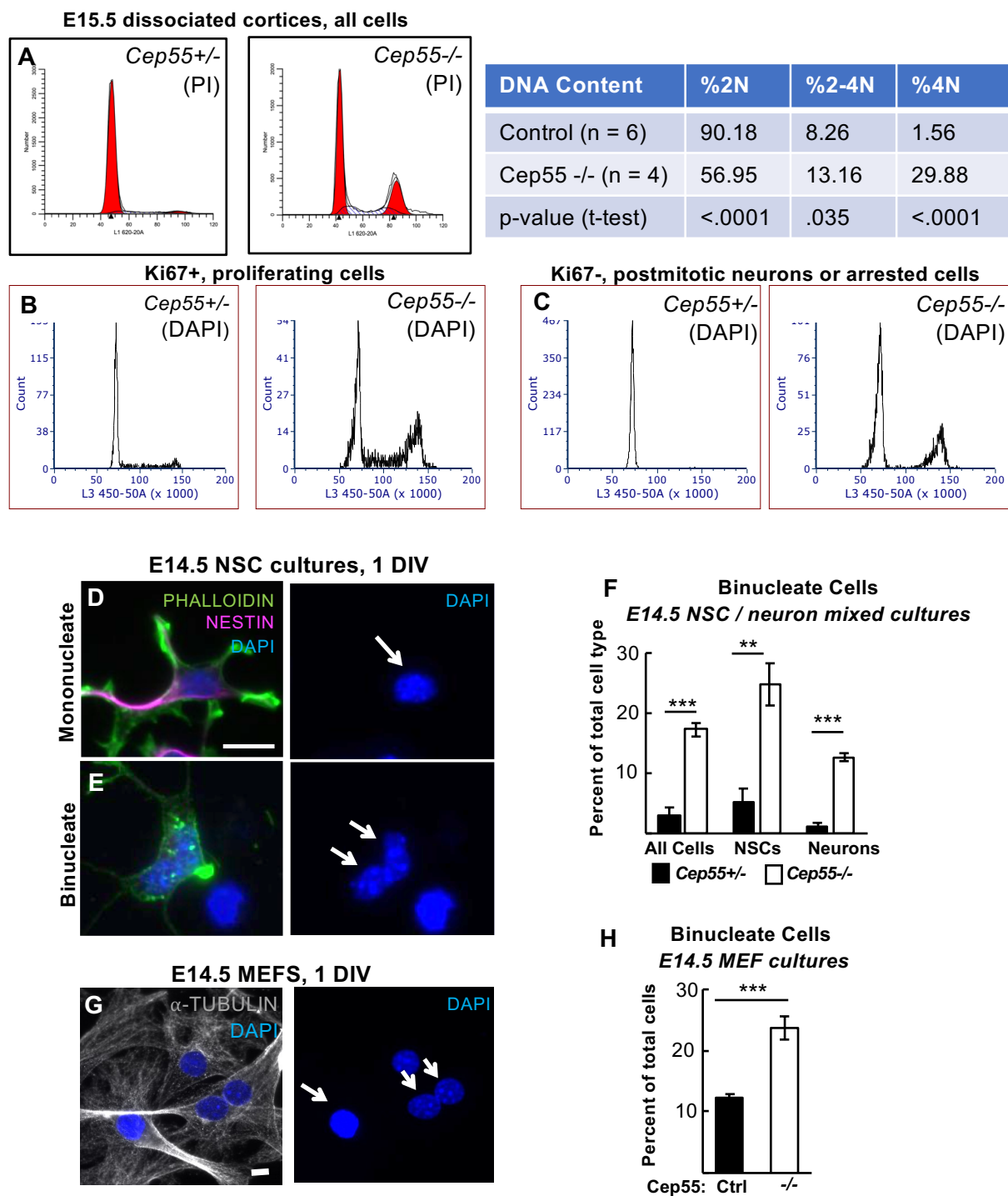339   neurons contributes to impaired cortical growth.

Figure 7: *Cep55* knockout mice have increased numbers of binucleate cortical cells and MEFs.
(A) Flow cytometric analysis of E15.5 dissociated cortices labeled with propidium iodide (PI) indicates an increase in cells with tetraploid (4N) DNA content in *Cep55-/-* brains, and concomitant decrease in cells with 2N DNA content. **(B-C)** Both proliferating (Ki67+) and non-proliferating (Ki67-, presumed neurons) populations of *Cep55-/-* brains show increases in 4N DNA cells. **(D-F)** Increased numbers of binucleate progenitors (Nestin+) and neurons (Nestin-) are seen in *Cep55-/-* dissociated cortical cultures at 1 day in vitro (DIV). D, arrow: example of mononucleate progenitor. E, arrow: example of binucleate neuron. **(G-H)** Primary cultures of mouse embryonic fibroblasts (MEFs) from *Cep55-/-* embryos have twice as many binucleate cells as control cultures at 1DIV. Arrow: example of mononucleate cell, double arrow: example of binucleate cell. For (A) n= 6 *Cep55+/+;+/-*, 4 *Cep55-/-* dissociated cortices; (B-C) n= 5 *Cep55+/+;+/-*, 5 *Cep55-/-* dissociated cortices; (F) n= 4 *Cep55+/+;+/-* and 4 *Cep55-/-* coverslips from 2 embryos each. (H) n=5 *Cep55+/-,* 5 *Cep55-/-* coverslips from 3 embryos each. n.s.; ** p < 0.01; *** p < 0.001. Scale bars in D and G, 10 µm.
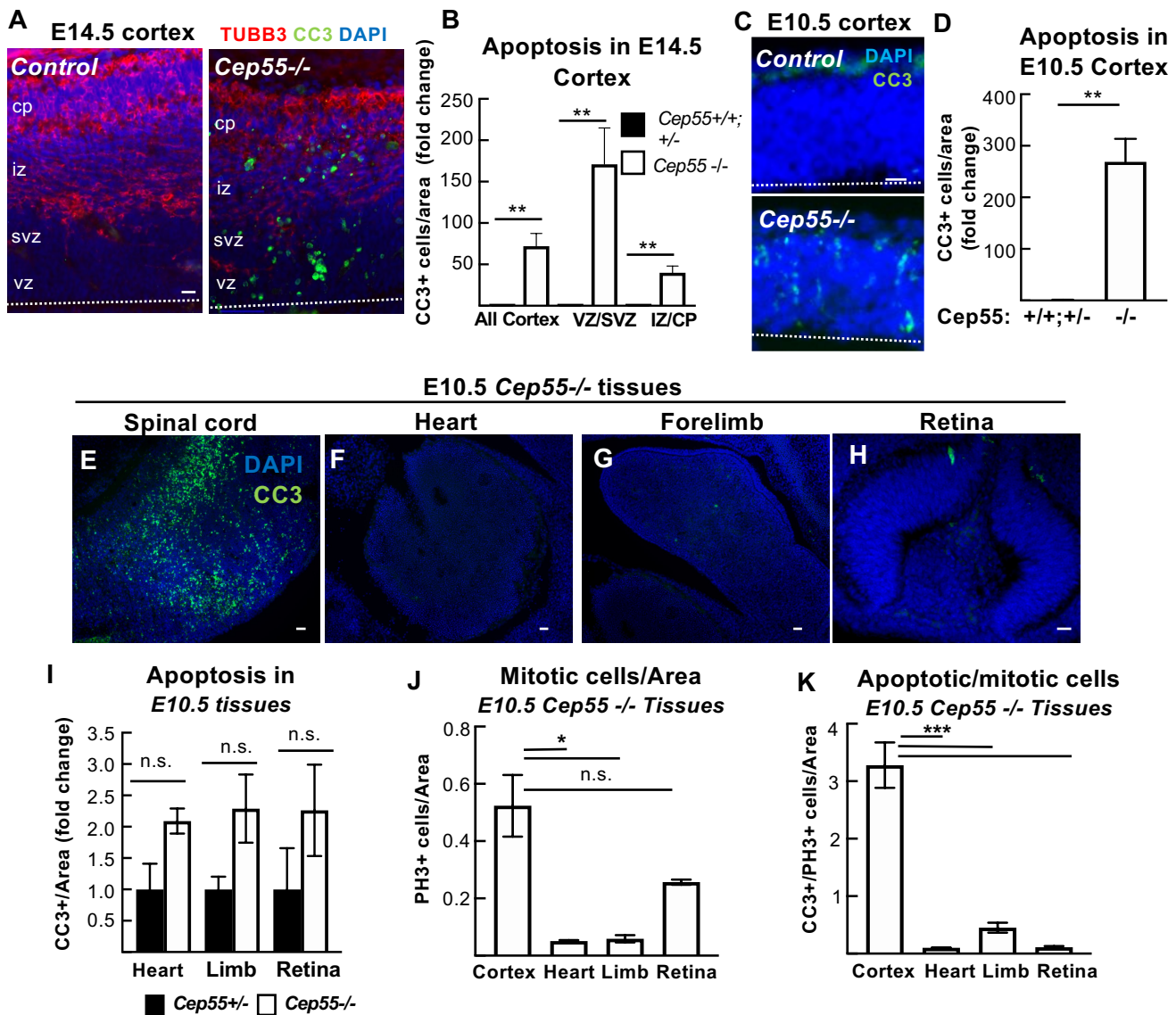
Figure 8: Apoptosis is greatly increased in the neural tissue of *Cep55* knockout embryos.
(A) Cortical sections immunostained for apoptotic cell marker cleaved-caspase 3 (CC3, green) show almost no CC3+ cells in control but many in *Cep55-/-* cortex. **(B)** At E14.5, apoptotic cells were most increased in the vz/svz, containing nuclei of NSCs and BPs, but also increased in neurons in cp/iz of -/- brains. **(C-D)** At E10.5, prior to neurogenesis, apoptosis is greatly increased in -/- forebrain NSCs. **(E-I)** Apoptosis is high in the E10.5 -/- spinal cord, (and midbrain and hindbrain, not shown), but not in heart, forelimb, or retina. **(J-K)** The brain specificity of the apoptosis is not simply due to higher mitotic index. Dashed line in A,C = apical membrane. For all experiments, n = 3 control and -/- brains or embryos at each age. Scale bars: (A): 20 μm (C): 20 μm, (D): 40 μm, (E): 40 μm, (I) 20 μm. * p <0.05, ** p < 0.01, *** p < 0.001. n.s., not significant. All experiments, Student's t-test.

340   We wondered whether a lack of apoptosis in non-cortical tissues could explain the less severe

341   body size in *Cep55 -/-* mice compared to brain size. Alternatively, apoptosis could occur in these tissues,

342   but proliferation increases to compensate. To address this question, we labeled E10.5 whole-embryo

343   sections with CC3. Interestingly, apoptosis is observed throughout central nervous system tissues **(Figure**

344   **8E**, spinal cord, and hindbrain and midbrain, not shown**)** but is not seen in the rest of the body, including

345   the heart precursor **(Figure 8F)**, the forelimb **(Figure 8G)**, and the retina **(Figure 8H)**; quantification

346   **(Figure 8I)**. There are many more mitotic cells in the developing cortex than in these tissues in both

347   controls (data not shown) and *Cep55 -/-* mice **(Figure 8J)**; however, even when normalized to the number

348   of mitotic cells, apoptosis is specifically increased in the *Cep55 -/-* cortex, not in the other tissues **(Figure**

349   **8K)**. These data suggest the interesting possibility that a distinct apoptotic response occurs in central

350   nervous system tissues after *Cep55* loss, that does not occur in all proliferating tissues.

351

352   **p53 nuclear expression is increased in *Cep55* knockout binucleate cortical cells, but not in**

353   **binucleate MEFs**

354

355   We previously showed that NSC apoptosis in a different abscission mutant, in the kinesin Kif20b,

356   was mediated by the tumor suppressor p53 (Little & Dwyer, 2019). To determine whether p53 elevation

357   occurs in *Cep55 -/-* cortices, we labeled E14.5 cortical sections with antibodies to p53. Indeed, while

358   virtually no cells with bright nuclear p53 accumulation are observed in control sections, greatly increased

359   numbers of p53+ cells are seen in *Cep55 -/-* sections **(Figure 9A-B)**. We noticed these cells throughout

360   the cortex, but especially increased in proliferative zones (vz/svz). While some p53 positive cells appear

361   singular, others appear paired **(Figure 9A, arrows)**. To further delineate in which *Cep55 -/-* cells p53

362   expression occurred, we used dissociated cortical cell cultures. We observed a 5-fold increase in the

363   number of cells with a nuclear:cytoplasmic (N:C) ratio of 2 or greater, indicative of p53 activation as it

364   acts in the nucleus **(Figure 9C-D)**.

365   Interestingly, just as apoptosis is increased in both NSCs and neurons in *Cep55 -/-* cortex, we

366   found increased nuclear p53 expression in both cell types **(Figure 9D).** While cytokinetic defects would

367   occur only in dividing NSCs, we reasoned that a failed cytokinesis event could result in the formation of a

368   binucleate daughter cell, either progenitor cell or neuron. Indeed, we had observed both binucleate NSCs

369   and neurons in *Cep55 -/-* cultures **(Figure 7F)**. To investigate if binucleation was associated with p53

370   activation and apoptosis in progenitor cells and neurons, we co-labeled cells with Nestin, Phalloidin and

371   p53. Indeed, there is an increased nuclear:cytoplasmic ratio of p53 expression in binucleate *Cep55 -/-*

372   NSCs and neurons compared to mononucleate cells **(Figure 9E)**. Furthermore, almost no mononucleate

373   cells have p53 N:C ratios > 2, while more than 50% of binucleate progenitors and 20% of binucleate
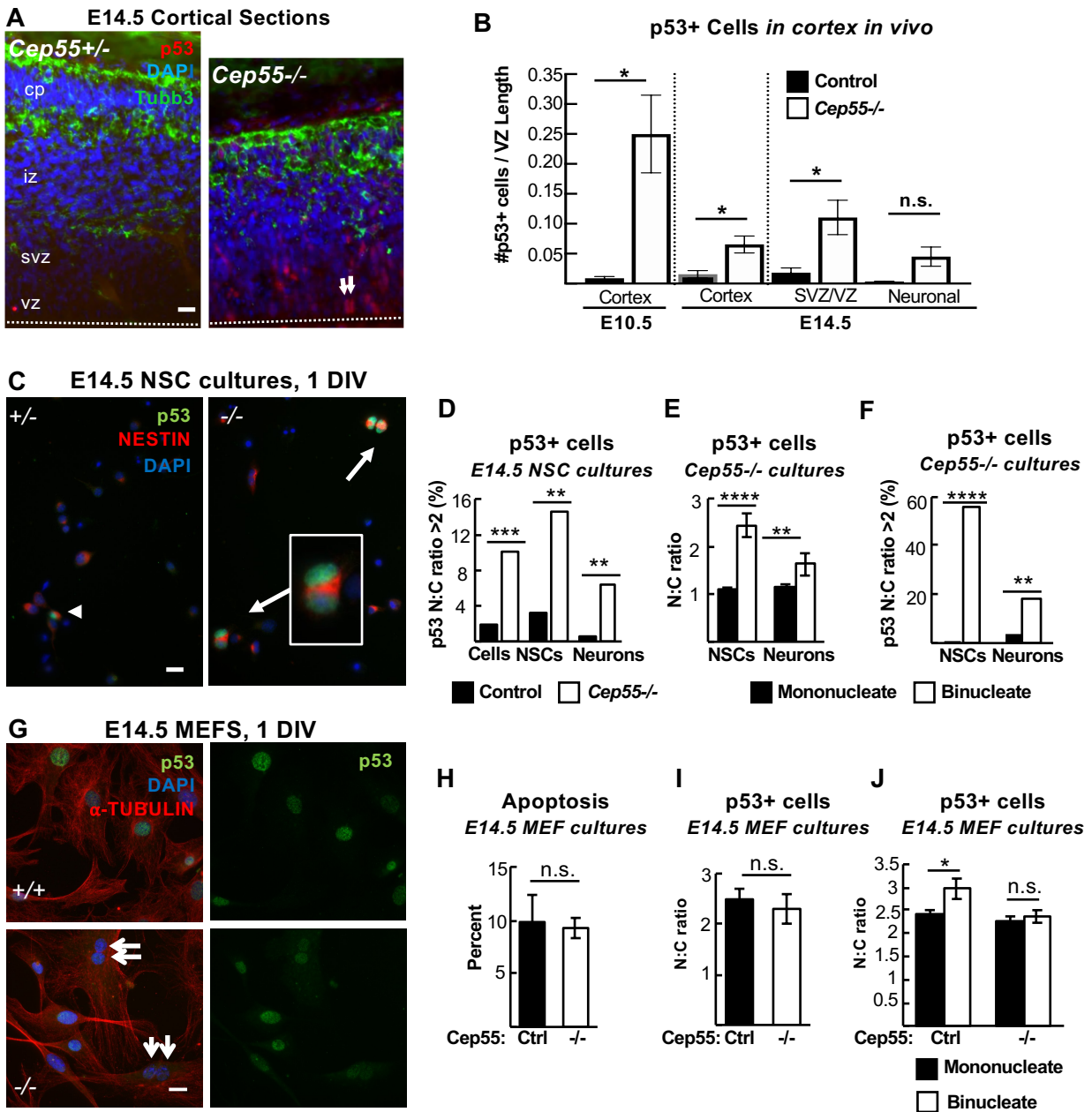
Figure 9. p53 nuclear accumulation is increased in *Cep55* knockout binucleate NSCs and neurons, but not in binucleate MEFs.

(A-B) Cortical sections immunostained for p53 and Tubb3 show almost no p53+ cells in controls but many in *Cep55-/-* cortices. Arrows, paired nuclei with p53 expression. **B.** p53+ cell counts are increased in *Cep55-/-* cortices at E10.5, and at E14.5, mostly in the vz/svz than neuronal layers **(C)** Images of dissociated NSC cultures show p53+ binucleate NSCs from *Cep55 -/-* cortices. **(D)** Counts of cells with a p53 nuclear:cytoplasmic (N:C) ratio of >2 are greatly increased in -/- cultures, both NSCs and neurons. **(E-F)** In Cep55 -/- NSC cultures, the mean N:C ratio of p53 intensity is about 1 in mononucleate NSCs or neurons, but significantly higher in binucleate progenitors and neurons. **(F)** In *Cep55-/-* cultures, over half of binucleate NSCs have a p53 N:C ratio > 2, compared to only 1% of mononucleate NSCs. Among binucleate neurons, ~ 20% have a p53 N:C ratio of >2 versus only 2% of mononucleate neurons. **(H)** Apoptosis (CC3+) is not increased in *Cep55-/-* primary MEF cultures compared to controls. **(I)** The N:C ratio of p53 signal (p53, green, G) is not different in -/- MEFs compared to controls. **(J)** Binucleate *Cep55 -/-* MEFs did not have an increased p53 N:C ratio compared to mononucleate -/- MEFs (G, arrows). Dashed line in A = apical membrane For B, n = 3 Cep55+/+;+/- and 3 Cep55 -/- mice at each age. For D-F, n= 4 Cep55+/+;+/- and 4 Cep55-/- coverslips from 2 embryos each; 124 control and 137 -/- NSCs; 143 -/- and 184 -/- neurons for N:C ratios. For H, n= 3 control and 3 Cep55-/- coverslips from 3 embryos each. For I, n= 195 control and 232 -/- cells from 3 control and Cep55-/- coverslips and embryos each. For J, n= 153 mononucleate and 25 binucleate control cells and 158 mononucleate and 68 binucleate -/- cells from 3 coverslips and 3 embryos each. Scale bars in A, C, G represent 20 μm. * p < 0.05; ** p < 0.01; *** p < 0.001; **** p < 0.0001, t-test.

374 neurons do **(Figure 9F)**. These data suggest the existence of a p53-dependent pathway for apoptosis of

375 binucleate cells in the cortex, that may be most sensitive in NSCs.

376   Our previous figures showed that apoptosis is increased in the brain but not body tissues of *Cep55*

377 knockouts. *Cep55 -/-* MEFs have defective ESCRT recruitment during abscission, and increased

378 binucleation. Therefore, we asked whether they also had increased p53 expression or apoptosis.

379 Surprisingly, the answer appears to be no, neither apoptosis nor p53 levels are increased in *Cep55 -/-*

380 MEF cultures **(Figure 9G-I)**. Furthermore, binucleate *Cep55 -/-* MEFs do not have any detectable

381 difference in p53 expression compared to mononucleate MEFs **(Figure 9J)**. These data suggest the

382 possibility that the p53-dependent apoptotic response to binucleation/tetraploidy, and/or its consequences,

383 is regulated differently in various cell types, contributing to the dramatic tissue-level differences in

384 phenotypic severity observed in germline *Cep55* knockouts.

385

386 ***Cep55* knockout forebrain apoptosis and size but not body size and longevity are p53-dependent.**

387

388   To test the hypothesis that p53 activation is the cause of apoptosis and microcephaly in *Cep55 -/-*

389 mice, we crossed the *p53* knockout to the *Cep55* knockout. Mouse knockouts of *p53* have normal brain

390 size and structure at birth, with almost no consequences for development (Insolera et al., 2014; Jacks et

391 al., 1994). As expected, *Cep55 -/-* mice with wild-type p53 status exhibit microcephaly **(Figure 10A,**

392 **second panel)**. We detected no difference in brain size with heterozygous deletion of p53 **(Figure 10A,**

393 **third panel)**. However, complete deletion of p53 partially rescues brain size **(Figure 10A, right-most**

394 **panel), and B, C)**. *Cep55;p53* double knockout cortical length is 21% longer than *Cep55 -/-* , but still

395 10% shorter than wild-type controls **(Figure 10B)**. Furthermore, cortical area is 32% larger than *Cep55 -*

396 */-*, but still 19% smaller than wild-type controls **(Figure 10C)**. Next, we evaluated whether deletion of

397 p53 prevents apoptosis in the *Cep55* knockout. Indeed, apoptosis in *Cep55 -/-* mice is p53-dependent

398 **(Figure 10D-E).** Therefore, preventing apoptosis partially rescues brain size in *Cep55 -/-* mice, but not to

399 wild-type size. These results highlight the importance of Cep55 function for sufficient NSC proliferation,

400 as even with apoptosis inhibition in *Cep55* knockouts brain growth is impaired.

401   We earlier noted that *Cep55 -/-* mice suffer postnatal lethality starting in the second week of life,

402 and have reduced body size at birth and poor postnatal growth **(Figure 1 – supplemental figure 1A, B)**.

403 Therefore, we wanted to investigate whether lethality or body size are improved in *Cep55;p53 -/-* mice, as

404 brain size is. Surprisingly, the postnatal survival curve of *Cep55;p53 -/-* mice is not improved compared

405 to *Cep55 -/-* single knockouts **(Figure 10F)**. Furthermore, body weight and size are still severely reduced

406 in *Cep55;p53 -/-* pups, similar to *Cep55 -/-* **(Figure 10G, H)**. Thus, it appears there are disparities in both
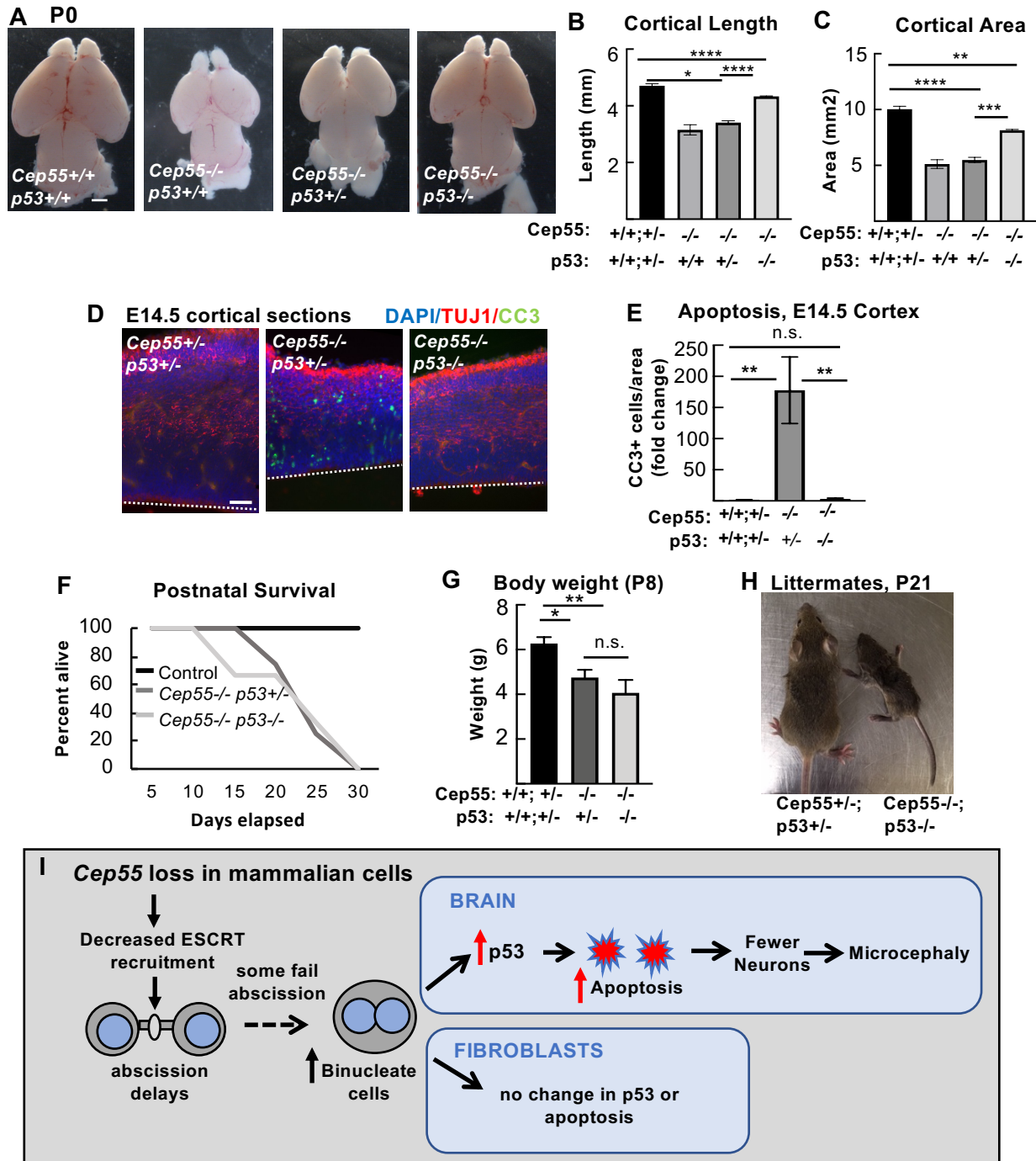
Figure 10. *p53* deletion blocks apoptosis and partially rescues brain size, but not body size or survival in *Cep55* knockout pups.
(A-C) Co-deletion of *p53* partially rescues microcephaly in *Cep55 -/-* mice. **(B-C)** Homozygous *p53* knockout shows partial rescue of *Cep55-/-* cortical length and area. **(D-E)** Apoptosis of *Cep55-/-* cortex is fully blocked in *Cep55;p53* double knockouts. Dashed line in D = apical membrane. **(F-H)** *p53* co-deletion does not improve *Cep55-/-* pups' postnatal survival (F) or body weight (G,H). For B,C; n=11 controls (*Cep55+/+,+/-; p53+/+,+/-),* 2 *Cep55-/-;p53+/+,* 5 *Cep55-/-;p53+/-,* 3 *Cep55-/-;p53-/-.* For E, n=3 controls *Cep55+/+,+/-; p53+/+,+/-,* 2 *Cep55-/-;p53+/+,* 3 *Cep55-/-;p53-/-.* For F and G, n=15 controls, 4 *Cep55+/-;p53-/-* and 3 *Cep55-/-;p53-/-.* * p <0.05, ** p < 0.01, *** p < 0.001, **** p <0.0001, n.s., not significant. B,C,F: one-way ANOVA. E: one-way ANOVA, Tukey's multiple comparisons test. **(I)** Working model for the effects of *Cep55* loss on abscission of mammalian cells, and for the differential effects on neural stem cells versus fibroblasts. *Cep55-/-* mouse cells have impaired ESCRT recruitment and abscission delay. Most cells complete abscission, but at least some fail to complete cytokinesis resulting in increased binucleate cells. Binucleate NSCs and neurons have elevated p53 expression, but not binucleate MEFs. p53 activation in NSCs and neurons causes apoptosis in Cep55 ko cortices, which partially accounts for microcephaly.

407   the consequences of *Cep55* loss for development of different tissues in the animal, and in the degree to

408   which p53 co-deletion rescues brain versus body size.

409

410   **Discussion**

411   In this work we investigated the roles of the cytokinetic abscission regulator Cep55 in embryonic

412   development, particularly in the brain. Data from cell lines had led to a general model in vertebrate cells

413   that Cep55 was critical for the recruitment of ESCRT components to the midbody, to complete

414   abscission. It was perhaps expected that knockout of Cep55 would cause early embryonic lethality, as

415   knockout of another cytokinesis gene, mgcRacGAP does (Van de Putte et al., 2001). However, we find

416   that while some cells fail abscission in the absence of Cep55, most succeed, and embryos develop and

417   survive past birth. ESCRT recruitment is indeed severely reduced in most *Cep55 -/-* midbodies, but it is

418   not abolished. We find Cep55 acts to ensure the speed and success rate of abscission **(Figure 10 I).** This

419   function of Cep55 appears to be especially important in NSCs, because it is essential for proper brain

420   growth. NSCs that fail abscission and become binucleate activate p53 and apoptosis, but embryonic

421   fibroblasts do not. Consistent with this, p53 co-deletion to prevent apoptosis partially rescues *Cep55 -/-*

422   brain size, but not body size. Our work emphasizes the need for understanding specialized requirements

423   for abscission regulation in different types of stem cells and growing tissues, and tissue-specific apoptotic

424   responses to abscission stress.

425   Knockout of *Cep55* enabled us to test the model that Cep55 is required to recruit ESCRT

426   components to the midbody, via interactions with Alix and Tsg101 (Carlton et al., 2008; Carlton &

427   Martin-Serrano, 2007; Lee et al., 2008; Morita et al., 2007; Stoten & Carlton, 2018) and that this

428   recruitment is necessary for abscission completion. Abscission includes both membrane scission and

429   microtubule disassembly to sever the intracellular bridge; ESCRT components, recruited by Cep55, are

430   thought to be necessary to couple these processes together temporally, by directly mediating membrane

431   scission and recruiting the microtubule-severing protein spastin (Guizetti et al., 2011; Steigemann et al.,

432   2009). Our findings appear to challenge two aspects of this model. First, we find correctly localized

433   ESCRT components in some *Cep55 -/-* midbodies, suggesting Cep55 is not the sole recruiter of ESCRTs

434   to the midbody in vertebrate cells. Second, we find that without Cep55, microtubule disassembly during

435   abscission does not fail but is only delayed. In HeLa cell cultures, Cep55 depletion caused greatly

436   increased midbody index, and cells remained at midbody stage for hours before either regressing or

437   finally succeeding (Fabbro et al., 2005; Zhao et al., 2006). By contrast, in NSCs *in vivo*, we only observed

438   a small increase in midbody index, and only a slight delay in microtubule disassembly in *Cep55 -/-* brains.

439   These findings suggest the intriguing possibility that microtubule disassembly and membrane scission are

440   uncoupled in the *Cep55 -/-* mouse, and that membrane scission is more severely delayed. It is possible

441   that microtubule severing proteins could be recruited through post-translation modifications of tubulin

442   instead of via ESCRTs (McNally & Roll-Mecak, 2018). This could explain why we observe excess

443   MBRs at the apical membrane in knockout brains: they could be tethered by a hollow membrane bridge.

444   Alternatively, increased MBRs in *Cep55 -/-* mice could indicate a problem in MBR disposal or

445   engulfment, as MBRs can bind to cell receptors and be internalized, influencing downstream cell polarity

446   and fate (Peterman et al., 2019; Pollarolo et al., 2011; Singh & Pohl, 2014). Clearly, more work is needed

447   to refine the general abscission model to determine the exact roles of Cep55 at the molecular level, the

448   mechanisms that may recruit ESCRT proteins besides Cep55, and whether either membrane scission or

449   microtubule disassembly can be achieved without ESCRT components.

450   Tissue-specific p53-dependent responses appear to be a major factor in the disproportionate

451   consequence of Cep55 loss for brain size compared to the rest of the body. This is consistent with recent

452   evidence for variable sensitivity of different murine developing tissues to p53 activation (Bowen et al.,

453   2019), and differential p53-dependent responses to cell stress in specific cell contexts (Kastenhuber &

454   Lowe, 2017). First, we find increased p53 expression and apoptosis in *Cep55 -/-* binucleate NSCs, but not

455   binucleate MEFs. Second, apoptosis is increased in *Cep55 -/-* CNS tissues, but not in other embryonic

456   body tissues. Finally, we show prevention of p53-dependent apoptosis partially rescues brain size in

457   *Cep55 -/-* mice, but does not improve body size or survival. It is likely that in multiple *Cep55 -/-* cell

458   types, abscission delays and failures hinder proliferation, resulting in decreased growth of body tissues,

459   but that in NSCs they additionally result in p53-dependent apoptosis. The explanation for this might be

460   that some tissues have a higher tolerance for abnormal cells. Indeed, some mammalian tissues, such as the

461   liver and heart, have binucleate cells normally (Guidotti et al., 2003; Paradis et al., 2014); and syncytia

462   development by incomplete cytokinesis is part of testis development (Greenbaum et al., 2011; Ren &

463   Russell, 1991). The brain appears to have a low threshold for damaged cells to activate p53; several

464   microcephalies involve p53-dependent apoptosis (Bianchi et al., 2017; Houlihan & Feng, 2014; Insolera

465   et al., 2014; Little & Dwyer, 2019; Mao et al., 2016). Since cortical NSCs undergo many rounds of cell

466   divisions to stochastically create lineage trees of different daughter cell types (Dwyer et al., 2016; Llorca

467   et al., 2019), even low rates of errors early in development can have profound effects on neuron

468   production and brain growth.

469   *Cep55* mutants serve as models for an emerging spectrum of human brain malformations. Human

470   mutations in *Cep55* also cause severe defects in CNS development and surprising relative sparing of other

471   tissues. Different alleles identified so far seem to cause a range of phenotypic severity. Null (nonsense)

472   mutations result in lethal hydranencephaly, a fluid-filled skull with almost no brain tissue (Bondeson et

473   al., 2017; Frosk et al., 2017; Rawlins et al., 2019). Compound heterozygotes for one nonsense allele and

474   one missense allele have microcephaly, a small brain with normal structure. Finally, splicing mutations in

475   *Cep55* result in micro-lissencephaly, a small brain with fewer sulci and gyri. The latter two classes of

476   patients survived (Barrie et al., 2020). Unlike humans and mice with *Cep55* mutations, a zebrafish *Cep55*

477   mutant has small eyes (Jeffery et al., 2015; Yanagi et al., 2019). The developing eye is a neuroepithelium

478   with NSCs that are similar to those in the brain, so it is unclear why the human and mouse do not have

479   small eyes upon *Cep55* loss. A possible explanation is that fish have larger eyes than forebrains, so their

480   eye growth may require the abscission speed and accuracy that Cep55 ensures. Together these data

481   suggest Cep55 may have evolved in vertebrates to help build bigger more complex nervous systems.

482   During the writing of this manuscript, another research group published the phenotype of a *Cep55*

483   knockout mouse (Tedeschi et al., 2020). They similarly found *Cep55 -/-* mice have microcephaly

484   disproportionate to body size reduction, an accumulation of binucleate NSCs, and apoptosis specific to

485   neural tissues. However, we performed additional analyses that cause us to differ with some of their

486   interpretations. First, we differ in that we find ESCRTs are sometimes recruited in *Cep55 -/-* cells. We are

487   the first two groups to attempt to answer this question quantitatively, and more work is needed by cell

488   biologists to determine if and how ESCRTs can be recruited without Cep55 in vertebrate cells. Second,

489   we show specific abscission defects occur in *Cep55 -/-* cortices, not simply binucleate cells: we find

490   abscission delay, midbody structural defects, and MBR accumulation in our *in vivo* brain

491   analyses. Importantly, we are the first to show Cep55 is not required for microtubule disassembly during

492   abscission. Future work will determine if *Cep55 -/-* NSCs are completing abscission without ESCRT

493   components, or whether recruitment is simply reduced or delayed. Third, we do find evidence of a role for

494   Cep55 in abscission of non-neural cell divisions, suggesting that Cep55 and the ESCRT system are not

495   dispensable for non-neural cells. Finally, we identify contrasting p53 responses to cytokinetic defects in

496   different cell types as a potential mechanism leading to disparate secondary consequences and tissue

497   phenotypes. Our data suggest that cell division defects and apoptosis are related, with increased p53

498   expression occurring in binucleate *Cep55 -/-* cortical cells. Future work by many groups with

499   complimentary approaches will be needed to understand Cep55 knockout phenotypes, why Cep55

500   evolved in vertebrates, and the complex regulation of cytokinesis in developing tissues.

501

502   **Materials and Methods**

503

504   *Mice*

505

506   Mouse colonies were maintained in accordance with NIH guidelines and policies approved by the
507   IACUC. Embryos were harvested by cesarean section, and the morning of the vaginal plug was
508   considered E0.5. Littermate embryos served as controls for all experiments and all parent and embryo
509   genotypes were confirmed by PCR. The Cep55 allele (strain C57BL/6NCep55$^{\text{em1(IMPC)Tcp}}$ was made as
510   part of the KOMP2 phase 2 project at the Toronto Centre for PhenoGenomics for the Canadian Mouse
511   Mutant Repository. It was maintained on C57BL/6 and 50/50% C57BL/6 and FVB/N background

512 embryos, which were used for experiments. We verified the correct mutation in our mutants with DNA
513 sequencing and RT-PCR (data not shown). p53 knockout (Trp53^{tm1Tyj}) mice on C57BL/6 background
514 were obtained from The Jackson Laboratory [(Jacks et al., 1994); JAX stock #002101 The Jackson
515 Laboratory Bar Harbor, ME]. These mice were bred with 50/50% C57BL/6 and FVB/N Cep55 knockout
516 embryos for creation of the Cep55;p53 mouse line. Cep55 heterozygous mice were crossed with both the
517 mT/mG reporter line (JAX stock #007576, The Jackson Laboratory Bar Harbor, ME) and Sox2-Cre mice
518 (JAX stock #0085454, The Jackson Laboratory Bar Harbor, ME(Hayashi et al., 2002; Muzumdar et al.,
519 2007) to produce mice that express plasma membrane-localized GFP. Sex of embryonic mice were not
520 noted as sex was not a relevant biological variable for these experiments. The specific ages of embryonic
521 mice used is noted in figure legends for each experiment.
522
523 For survival analyses, pups were kept with their mother and littermates. Milk was noted in the bellies of
524 Cep55 -/- and Cep55;p53 double knockout mice until at least P2. Pups were weaned at 21-25 days, unless
525 too small to be separated from mothers. In some situations, pups were euthanized due to severe failure to
526 thrive for humane reasons, and that was recorded as the day of death; in most cases pups died without
527 intervention.
528
529 *Immunoblotting*
530
531 MEF cells were washed with ice cold PBS, and lysed directly on the plate (6cm) into lysis buffer (500
532 µl); 50mM Tris HCl, 150mM NaCl, 1% NP-40, 1mM EDTA, 1mM DTT, 1mM PMSF, 1X HALT
533 protease/phosphatase inhibitor cocktail. After incubating lysates on a rotisserie at 4° C for 30 minutes,
534 lysate were cleared by centrifugation at 21k x g for 15 min at 4° C. Supernatants were diluted to 1x with
535 5X Laemmli buffer for western blot. Equivalent amounts of cells within each experiment were run on a 4-
536 20% polyacrylamide gel. After transfer onto nitrocellulose with the BioRad Transblot Turbo, membrane
537 was blocked with Licor TBS blocking buffer for 1 hour at room temp. Primary and secondary antibodies
538 were diluted in 50% blocking buffer, 50% TBS, final 0.1% Tween-20. Primary antibodies were
539 incubated overnight at 4° C, and after washing, followed by appropriate species specific near-infrared
540 (680 or 800nm) secondary antibodies for 1 hour at room temperature. Blots were imaged with the dual
541 color Licor Odyssey CLx imager. Densitometry of western blots was performed with Licor Image Studio
542 software. Primary antibodies used: rabbit monoclonal anti human beta-actin (1:10,000, Clone13E5 4970
543 Cell Signaling, Danvers, MA) and mouse monoclonal anti-mouse Cep55 raised against amino acids 163-
544 462 mapping at the C-terminus (1:1000, sc-377018 Santa Cruz, Dallas, Texas).
545
546 *Immunostaining and H&E Staining*
547
548 To collect cryosections for immunohistochemistry in supplemental figure 2, and figures 3, 5, 9, 10 and
549 11, age E12.5, E14.5 and P0 brains were removed from heads and fixed for 4, 6 and 24 hours,
550 respectively, in 4% PFA, followed by immersion in 30% sucrose in PBS overnight. Whole E10.5
551 embryos (used in figure 9) were fixed overnight. Next, whole brains or embryos were embedded in
552 O.C.T. compound (Tissue-Tek 4583, Sakuraus Torrance, CA) and cryosections were cut at 20 µm
553 thickness and collected on Superfrost Plus slides (Fisher Scientific, 12–550-15). Frozen sections were
554 stored at −80 degrees. Prior to immunostaining, cryosections were warmed to room temperature, then if
555 antigen retrieval was needed (Pax6, Tbr2, p53 antibodies), immersed in 10 mM citrate buffer at 95
556 degrees for 20 minutes. After cooling, sections were blocked in 2% NGS for 1 hour, followed by
557 incubation with primary antibodies overnight at 4 ° C. The next day, after PBS washes, sections were
558 incubated with AlexaFluor secondary antibodies at 1:200 and DAPI at 1:100 for 30 min followed by PBS
559 washes and coverslipping with VectaShield fluorescent mounting medium.
560
561 For immunofluorescence (IF) on coverslips of dissociated cortical progenitors and MEFs (figures 2, 6, 7,
562 and 10), a similar protocol was used but with primary antibodies applied for 3 h at room temperature.

563   Antigen retrieval was not used in dissociated progenitors except in the case of Tbr2 immunostaining;
564   coverslips were immersed in 0.07M NaOH pH 13 for 2 min before permeabilization. Coverslips were
565   mounted on Superfrost Plus slides with Fluoro-Gel (Electron Microscopy Sciences, Hatfield, PA, 17985–
566   10).

567
568   Paraffin-embedded brains were sectioned and stained with hematoxylin and eosin (H & E) by the UVA
569   Research Histology Core for Figures 1 and Supplemental Figure 2.

570
571   *Cortical cell cultures*

572
573   Cells were dissociated from E14.5 cortices following a protocol adapted from Sally Temple's laboratory
574   (Qian et al., 1998). The Worthington Papain Dissociation Kit was used to dissociate cells (Worthington
575   Biochemical Corporation, Lakewood, NJ, Cat # LK003150). Cells were cultured in DMEM with Na-
576   Pyruvate, L-Glutamine, B-27, N2, N-acetyl-cysteine and basic fibroblast growth factor (Final Culture
577   Media). After 24 or 48 hrs, cells were fixed by adding an equal volume of room temperature 8% PFA
578   (paraformaldehyde) for 5 min to cell media, followed by removal of media and addition of −20° cold
579   methanol for 5 min.

580
581   *Mouse embryonic fibroblast (MEF) cultures*

582
583   Embryos from timed pregnant females were collected at E14.5. Embryos were decapitated, internal
584   organs were removed from body cavities and remaining tissue was triturated with a 1 ml pipette and
585   incubated in 1ml of 0.25% trypsin-EDTA for 25min at 37°C. The tissue was further triturated and tubes
586   were spun at 1000 rpm for 5 min and the medium was aspirated off. The pellet was resuspended in
587   DMEM/20% FBS with pen/strep added. The resulting cells from each embryo were plated in two 10 cm
588   plates in DMEM/10% FBS. The next day, media was replaced. When approaching confluence, cells were
589   trypsinized and plated on fibronectin-coated coverslips, grown overnight, and fixed with 4%
590   paraformaldehyde (PFA) for 10 minutes or cold methanol for 10 minutes at 24 or 48 hrs.

591
592   *Cortical slabs for apical membrane view*

593
594   Cortical slabs were prepared as previously described (Janisch & Dwyer, 2016). The meninges and skull
595   were removed to expose the brain in E12.5 and E14.5 embryos, followed by fixation with 2% PFA for 20
596   min. Next, apical slabs were made by pinching off cortices, flipping so that the apical surface was upright,
597   and trimming to flatten the slab. Slabs were fixed for another 2 min with 2% PFA followed by blocking
598   with 5% normal goat serum (NGS) for 1 h. Primary antibodies were applied for 1 h at room temperature
599   and then moved to 4° overnight. The next day, after 3 times, 10-minute PBS (phosphate-buffered saline)
600   washes, secondary antibodies and DAPI were applied at a concentration of 1:200 for 30 minutes. After
601   two more 10–minute PBS washes, slabs were coverslipped with VectaShield fluorescent mounting
602   medium (Vector Laboratories Inc., Burlingame, CA H-1000) and imaged. z-stack depth was 8–20 μm and
603   step size was 0.5 μm.

604
605   *Flow Cytometry*

606
607   Cells from E15.5 brains were dissociated using the Papain Dissociation Kit (Worthington Biochemical
608   Corporation). Single-cell suspensions were obtained by filtering through a 40 μm filter (BD Falcon Cell
609   Strainer, blue nylon mesh, catalog #352340). For propidium iodide (PI) staining, cells were resuspended
610   in 500 μl PBS and added to 4.5 ml ice-cold 70% ethanol for at least 2 hours. Samples were stored at 4°C.
611   Fixed cells were rinsed in PBS and resuspended in 1 ml solution containing 100 μg/ml RNase A, 0.1%
612   Triton X-100 and 50 μg/ml PI, and incubated at room temperature for 30 minutes in the dark. For Ki-67
613   and DAPI analysis, single-cell suspensions of E15.5 brains (*n*=3 pairs of *Cep55* mutants and littermate

controls) were fixed in 1.5% PFA for 15 minutes on ice. Cells were then washed twice with FACS buffer
(2% BSA, 1 mM EDTA, 0.01% sodium azide, PBS) and permeabilized in 0.1% Triton X-100 in PBS for
30 minutes on ice. Cells were washed twice in FACS buffer and 2×10^6 cells were incubated in 100 μl
FACS buffer with 1 μg/ml DAPI and 2 μl anti-Ki-67 antibody (monoclonal rat anti-Ki-67 Alexa Fluor
647, clone SolA15, eBioscience, Waltham, MA). Following three washes with FACS buffer, fluorescence
was measured using a FACSCanto II flow cytometer (Becton Dickinson, Franklin Lakes, NJ). At least
20,000 events were collected per sample. Data were analyzed using FlowJo software (TreeStar).

Abscission Live Imaging and Analysis

This method was previously described in (McNeely & Dwyer, 2020), based on first establishing SiR-
tubulin for abscission duration studies in HeLa cells (Janisch et al., 2018). Briefly, E13.5 slabs were
prepared as described above and placed apical surface down in a glass-bottom dish (MatTek, Ashland,
MA, P35G-1.0–20-C) containing 50 nM SiR-Tubulin (Cytoskeleton, Denver, CO CY-SC002) in Final
Culture Medium (described above). Each dish was placed in a humidifying chamber and into a 37 °C
incubator with 5% CO2 overnight (approximately 15 h). The next day, the cortices were removed from
the incubator, and prepared for imaging by adding Matrigel (Corning, Corning, NY, 356237; 1:3 dilution
in Final Culture Medium) and a coverslip (Fisher 12–545-100) over the top of the cortical slab explant.
Matrigel was allowed to solidify for 5 min in the incubator before final culture medium with 2% 4-(2-
hydroxyl)-1-piperazineethanesulfonic acid (Gibco, Waltham, MA 15630080) was added to the dish, and
then, imaging was performed. An Applied Precision (GE) DeltaVision with a heating plate and 40×
objective (numerical aperture 1.53) was used for time-lapse image acquisition; z stacks of images ~10-
μm deep (z steps 0.4 μm) were taken every 15 min for abscission for up to 6 h. To minimize
phototoxicity, the neutral density filter was set at 32% or lower, and the exposure time was kept to a
minimum (<0.1 ms per slice). Deconvolved full z stacks and maximum intensity projection images were
analyzed using ImageJ. For abscission duration, time 0 was midbody formation as ascertained by SiR-
Tubulin appearance (compact microtubule bundles). Abscission completion was scored as the time point
when there was complete removal of microtubules on a midbody flank ascertained when the SiR-Tubulin
signal intensity decreased to background level. Midbody membrane scission was shown to be temporally
coincident with midbody flank microtubule disassembly by several previous publications using
differential interference contrast or phase imaging of cell lines in two-dimensional dissociated cultures
(Elia et al., 2011; Lafaurie-Janvore et al., 2013; Steigemann et al., 2009); however here, we cannot rule
out the possibility that the midbody plasma membrane might remain connected for some period of time
after the microtubules are gone.

Antibodies

Antibodies used in this analysis: mouse monoclonal anti- mouse citron kinase (1:100, CITK; 611367 BD
Biosciences, San Jose, CA), mouse polyclonal anti-human Cep55 (1:00, H00055165-B01P Abnova,
Taipei, Taiwan), mouse monoclonal anti-mouse Cep55 (1:100 for immunofluorescence experiments, sc-
377018 Santa Cruz, , Dallas, Texas), rabbit polyclonal anti-human CC3 (1:250, 9661s Cell-Signaling,
Danvers, MA), rat monoclonal anti-mouse Tbr2 (1:200, 14-4875, eBioscience (Thermo Fisher Scientific),
Waltham, MA), rabbit polyclonal anti-mouse Pax6 (1:200, PRB-278P, BioLegend, San Diego, CA),
mouse monoclonal anti-rat Aurora B kinase (1:300, 611082 BD Biosciences, San Jose, CA), rabbit
monoclonal anti-human Aurora B kinase (1:100, ab2254, Abcam, Cambridge, MA), rat monoclonal
alpha-tubulin (1:300, NB600-506, Novus Biologicals, Centennial, CO), rabbit monoclonal anti-human
PH3 (1:200, 3458 Cell Signaling, Danvers, MA), chicken polyclonal anti-mouse Nestin (1:600, NES,
Aves Labs, Davis, CA), rat monoclonal anti-human Ki67 (1:100, 14-5698 eBioscience, Waltham, MA),
rabbit polyclonal anti-mouse p53 (1:500, NCL-L-p53-CM5p Leica Biosystems, Wetzlar, Germany), rat
monoclonal anti-human Ctip2 (1:400, 18465 Abcam, Cambridge, MA), rabbit polyclonal anti-mouse
Tbr1 (1:200, 31940 Abcam, Cambridge, MA), rabbit monoclonal Satb2 (1:200 Ab92446 Abcam,

665   Cambridge, MA), rabbit polyclonal pericentrin (1:500, 92371, BioLegend, San Diego, CA) , mouse
666   monoclonal Tubb3 (Tuj1) (1:500, 801201, BioLegend, San Diego, CA), mouse monoclonal phospho-
667   histone H3 (Ser10) (1:200, 9706, Cell Signaling, Danvers, MA), Phalloidin Oregon Green or 568 (1:50,
668   07466, Al2380 Invitrogen, Waltham, MA), chicken polyclonal anti-human alpha-tubulin (1:100, ab89984
669   Abcam, Cambridge, MA), mouse monoclonal Alix (1:100, SC-53538 Santa Cruz, Dallas, Texas), mouse
670   monoclonal Tsg101 (1:100, SC-7964 Santa Cruz, Dallas, Texas), rabbit polyclonal CHMP2A (1:100,
671   10477-1-AP Proteintech, Chicago, IL), rat monoclonal Zo-1 (1:50, R26.4DC, DSHB, Iowa City, IA) and
672   polyclonal rabbit anti Zo-1 (1:50 61-7300, rabbit, Invitrogen (Thermo Fisher Scientific), Waltham, MA).
673   All antibodies were validated for the application used in multiple previous publications.
674
675   *Imaging and statistical analysis*
676
677   Images used for data analysis in supplemental figures 2F-G, and figures 2C-E, 6, 9, 10 and 11 were
678   collected on either a Zeiss Axio ImagerZ1 microscope with AxioCam MRm or a Zeiss AxioObserver
679   fluorescent widefield inverted scope microscope. Images in figures 2A-B, 3, 4, 5A-B, 7 and 8 were taken
680   on an inverted DeltaVision with TrueLight deconvolution microscope with softWoRx Suite 5.5 image
681   acquisition software (Applied Precision (GE Healthcare), Issaquah, WA). A Leica MZ16F microscope
682   with DFC300FX camera was used for images in Figures 1 and 11A-C, and supplemental figures 1 and
683   2A-E. Control and mutant fluorescence images were collected with the same exposure times and on the
684   same day. All image analysis was performed in ImageJ/Fuji and any changes to brightness and contrast
685   were applied uniformly across images. Statistical analyses were performed using Excel (Microsoft) or
686   GraphPad PRISM software. The sample sizes were pre-determined based on our lab's previous
687   experience with cortical development analyses and others' published results. After obtaining pilot data,
688   power analyses were performed if necessary to determine if the number of samples obtained was high
689   enough for the effect size seen. NSC cultures that were unhealthy were not imaged and analyzed, but no
690   other data was excluded from the analysis. No randomization or blinding was used as no experimental
691   manipulation was applied other than genetic knockouts. Genotyping was performed after collection of
692   embryos to determine genetic status. Statistical tests used are specified in each figure legend. For each
693   sample set a statistical test of normality was performed using GraphPad PRISM software. Parametric tests
694   were used when sample sets had a normal distribution and non-parametric tests were used when sample
695   sets did not have a normal distribution. Variance was calculated and was typically similar between
696   groups.
697

707

708   **Competing interests**
709   The authors have no competing interests to declare.
710

711   **References**
712

713   Addi, C., Presle, A., Fremont, S., Cuvelier, F., Rocancourt, M., Milin, F., Schmutz, S., Chamot-Rooke, J.,
714   Douche, T., Duchateau, M., Giai Gianetto, Q., Salles, A., Menager, H., Matondo, M.,
715   Zimmermann, P., Gupta-Rossi, N., & Echard, A. (2020). The Flemmingsome reveals an ESCRT-

716   to-membrane coupling via ALIX/syntenin/syndecan-4 required for completion of cytokinesis. *Nat*
717   *Commun, 11*(1), 1941. doi:10.1038/s41467-020-15205-z
718   Barrie, E. S., Overwater, E., van Haelst, M. M., Motazacker, M. M., Truxal, K. V., Crist, E., Mostafavi,
719   R., Pivnick, E. K., Choudhri, A. F., Narumanchi, T., Castelluccio, V., Walsh, L. E., Garganta, C.,
720   & Gastier-Foster, J. M. (2020). Expanding the spectrum of CEP55-associated disease to viable
721   phenotypes. *Am J Med Genet A, 182*(5), 1201-1208. doi:10.1002/ajmg.a.61512
722   Bastos, R. N., & Barr, F. A. (2010). Plk1 negatively regulates Cep55 recruitment to the midbody to
723   ensure orderly abscission. *J Cell Biol, 191*(4), 751-760. doi:10.1083/jcb.201008108
724   Bianchi, F. T., Tocco, C., Pallavicini, G., Liu, Y., Verni, F., Merigliano, C., Bonaccorsi, S., El-Assawy,
725   N., Priano, L., Gai, M., Berto, G. E., Chiotto, A. M., Sgro, F., Caramello, A., Tasca, L., Ala, U.,
726   Neri, F., Oliviero, S., Mauro, A., Geley, S., Gatti, M., & Di Cunto, F. (2017). Citron Kinase
727   Deficiency Leads to Chromosomal Instability and TP53-Sensitive Microcephaly. *Cell Rep, 18*(7),
728   1674-1686. doi:10.1016/j.celrep.2017.01.054
729   Bondeson, M. L., Ericson, K., Gudmundsson, S., Ameur, A., Ponten, F., Wesstrom, J., Frykholm, C., &
730   Wilbe, M. (2017). A nonsense mutation in CEP55 defines a new locus for a Meckel-like
731   syndrome, an autosomal recessive lethal fetal ciliopathy. *Clin Genet, 92*, 510-516.
732   doi:10.1111/cge.13012
733   Bowen, M. E., McClendon, J., Long, H. K., Sorayya, A., Van Nostrand, J. L., Wysocka, J., & Attardi, L.
734   D. (2019). The Spatiotemporal Pattern and Intensity of p53 Activation Dictates Phenotypic
735   Diversity in p53-Driven Developmental Syndromes. *Dev Cell, 50*(2), 212-228 e216.
736   doi:10.1016/j.devcel.2019.05.015
737   Carlton, J. G., Agromayor, M., & Martin-Serrano, J. (2008). Differential requirements for Alix and
738   ESCRT-III in cytokinesis and HIV-1 release. *Proc Natl Acad Sci U S A, 105*(30), 10541-10546.
739   Carlton, J. G., & Martin-Serrano, J. (2007). Parallels between cytokinesis and retroviral budding: a role
740   for the ESCRT machinery. *Science, 316*(5833), 1908-1912. doi:10.1126/science.1143422
741   Chaigne, A., Labouesse, C., Agnew, M., Hannezo, E., Chalut, K. J., & Paluch, E. K. (2019). Abscission
742   couples cell division to embryonic stem cell fate. *BioRxiv*, 798165. doi:10.1101/798165
743   Christ, L., Raiborg, C., Wenzel, E. M., Campsteijn, C., & Stenmark, H. (2017). Cellular Functions and
744   Molecular Mechanisms of the ESCRT Membrane-Scission Machinery. *Trends Biochem Sci,*
745   *42*(1), 42-56. doi:10.1016/j.tibs.2016.08.016
746   Christ, L., Wenzel, E. M., Liestol, K., Raiborg, C., Campsteijn, C., & Stenmark, H. (2016). ALIX and
747   ESCRT-I/II function as parallel ESCRT-III recruiters in cytokinetic abscission. *J Cell Biol,*
748   *212*(5), 499-513. doi:10.1083/jcb.201507009
749   Connell, J. W., Lindon, C., Luzio, J. P., & Reid, E. (2009). Spastin couples microtubule severing to
750   membrane traffic in completion of cytokinesis and secretion. *Traffic, 10*(1), 42-56.
751   doi:10.1111/j.1600-0854.2008.00847.x
752   Crowell, E. F., Gaffuri, A. L., Gayraud-Morel, B., Tajbakhsh, S., & Echard, A. (2014). Engulfment of the
753   midbody remnant after cytokinesis in mammalian cells. *J Cell Sci, 127*(Pt 17), 3840-3851.
754   doi:10.1242/jcs.154732
755   Di Cunto, F., Imarisio, S., Hirsch, E., Broccoli, V., Bulfone, A., Migheli, A., Atzori, C., Turco, E., Triolo,
756   R., Dotto, G. P., Silengo, L., & Altruda, F. (2000). Defective neurogenesis in citron kinase
757   knockout mice by altered cytokinesis and massive apoptosis. *Neuron, 28*(1), 115-127.
758   Dwyer, N. D., Chen, B., Chou, S. J., Hippenmeyer, S., Nguyen, L., & Ghashghaei, H. T. (2016). Neural
759   Stem Cells to Cerebral Cortex: Emerging Mechanisms Regulating Progenitor Behavior and
760   Productivity. *J Neurosci, 36*(45), 11394-11401. doi:10.1523/JNEUROSCI.2359-16.2016
761   Dwyer, N. D., Manning, D. K., Moran, J. L., Mudbhary, R., Fleming, M. S., Favero, C. B., Vock, V. M.,
762   O'Leary, D. D., Walsh, C. A., & Beier, D. R. (2011). A forward genetic screen with a
763   thalamocortical axon reporter mouse yields novel neurodevelopment mutants and a distinct Emx2
764   mutant phenotype. *Neural Dev, 6*(1), 3.

Elia, N., Sougrat, R., Spurlin, T. A., Hurley, J. H., & Lippincott-Schwartz, J. (2011). Dynamics of endosomal sorting complex required for transport (ESCRT) machinery during cytokinesis and its role in abscission. *Proc Natl Acad Sci U S A, 108*(12), 4846-4851. doi:10.1073/pnas.1102714108

Ettinger, A. W., Wilsch-Brauninger, M., Marzesco, A. M., Bickle, M., Lohmann, A., Maliga, Z., Karbanova, J., Corbeil, D., Hyman, A. A., & Huttner, W. B. (2011). Proliferating versus differentiating stem and cancer cells exhibit distinct midbody-release behaviour. *Nat Commun, 2*, 503.

Fabbro, M., Zhou, B. B., Takahashi, M., Sarcevic, B., Lal, P., Graham, M. E., Gabrielli, B. G., Robinson, P. J., Nigg, E. A., Ono, Y., & Khanna, K. K. (2005). Cdk1/Erk2- and Plk1-dependent phosphorylation of a centrosome protein, Cep55, is required for its recruitment to midbody and cytokinesis. *Dev Cell, 9*(4), 477-488. doi:10.1016/j.devcel.2005.09.003

Frosk, P., Arts, H. H., Philippe, J., Gunn, C. S., Brown, E. L., Chodirker, B., Simard, L., Majewski, J., Fahiminiya, S., Russell, C., Liu, Y. P., Consortium, F. C., Canadian Rare Diseases, M., Mechanisms, N., Hegele, R., Katsanis, N., Goerz, C., Del Bigio, M. R., & Davis, E. E. (2017). A truncating mutation in CEP55 is the likely cause of MARCH, a novel syndrome affecting neuronal mitosis. *J Med Genet, 54*(7), 490-501. doi:10.1136/jmedgenet-2016-104296

Gao, L., Jia, G., Li, A., Ma, H., Huang, Z., Zhu, S., Hou, Y., & Fu, X. (2017). RNA-Seq transcriptome profiling of mouse oocytes after in vitro maturation and/or vitrification. *Sci Rep, 7*(1), 13245. doi:10.1038/s41598-017-13381-5

Goliand, I., Adar-Levor, S., Segal, I., Nachmias, D., Dadosh, T., Kozlov, M. M., & Elia, N. (2018). Resolving ESCRT-III Spirals at the Intercellular Bridge of Dividing Cells Using 3D STORM. *Cell Rep, 24*(7), 1756-1764. doi:10.1016/j.celrep.2018.07.051

Green, R. A., Paluch, E., & Oegema, K. (2012). Cytokinesis in animal cells. *Annu Rev Cell Dev Biol, 28*, 29-58. doi:10.1146/annurev-cellbio-101011-155718

Greenbaum, M. P., Iwamori, T., Buchold, G. M., & Matzuk, M. M. (2011). Germ cell intercellular bridges. *Cold Spring Harb Perspect Biol, 3*(8), a005850. doi:10.1101/cshperspect.a005850

Gruneberg, U., Neef, R., Li, X., Chan, E. H., Chalamalasetty, R. B., Nigg, E. A., & Barr, F. A. (2006). KIF14 and citron kinase act together to promote efficient cytokinesis. *J Cell Biol, 172*(3), 363-372. doi:10.1083/jcb.200511061

Guidotti, J. E., Bregerie, O., Robert, A., Debey, P., Brechot, C., & Desdouets, C. (2003). Liver cell polyploidization: a pivotal role for binuclear hepatocytes. *J Biol Chem, 278*(21), 19095-19101. doi:10.1074/jbc.M300982200

Guizetti, J., Schermelleh, L., Mantler, J., Maar, S., Poser, I., Leonhardt, H., Muller-Reichert, T., & Gerlich, D. W. (2011). Cortical constriction during abscission involves helices of ESCRT-III-dependent filaments. *Science, 331*(6024), 1616-1620.

Hayashi, S., Lewis, P., Pevny, L., & McMahon, A. P. (2002). Efficient gene modulation in mouse epiblast using a Sox2Cre transgenic mouse strain. *Mech Dev, 119 Suppl 1*, S97-S101.

Houlihan, S. L., & Feng, Y. (2014). The scaffold protein Nde1 safeguards the brain genome during S phase of early neural progenitor differentiation. *Elife, 3*, e03297. doi:10.7554/eLife.03297

Hu, C. K., Coughlin, M., & Mitchison, T. J. (2012). Midbody assembly and its regulation during cytokinesis. *Mol Biol Cell, 23*(6), 1024-1034.

Insolera, R., Bazzi, H., Shao, W., Anderson, K. V., & Shi, S. H. (2014). Cortical neurogenesis in the absence of centrioles. *Nat Neurosci, 17*(11), 1528-1535. doi:10.1038/nn.3831

Jacks, T., Remington, L., Williams, B. O., Schmitt, E. M., Halachmi, S., Bronson, R. T., & Weinberg, R. A. (1994). Tumor spectrum analysis in p53-mutant mice. *Curr Biol, 4*(1), 1-7.

Janisch, K. M., & Dwyer, N. D. (2016). Imaging and quantitative analysis of cytokinesis in developing brains of Kinesin-6 mutant mice. *Methods Cell Biol, 131*, 233-252. doi:10.1016/bs.mcb.2015.06.008

Janisch, K. M., McNeely, K. C., Dardick, J. M., Lim, S. H., & Dwyer, N. D. (2018). Kinesin-6 KIF20B is required for efficient cytokinetic furrowing and timely abscission in human cells. *Mol Biol Cell, 29*(2), 166-179. doi:10.1091/mbc.E17-08-0495

816 Janisch, K. M., Vock, V. M., Fleming, M. S., Shrestha, A., Grimsley-Myers, C. M., Rasoul, B. A., Neale,
817   S. A., Cupp, T. D., Kinchen, J. M., Liem, K. F., Jr., & Dwyer, N. D. (2013). The vertebrate-
818   specific Kinesin-6, Kif20b, is required for normal cytokinesis of polarized cortical stem cells and
819   cerebral cortex size. *Development, 140*(23), 4672-4682. doi:10.1242/dev.093286
820 Jeffery, J., Neyt, C., Moore, W., Paterson, S., Bower, N. I., Chenevix-Trench, G., Verkade, H., Hogan, B.
821   M., & Khanna, K. K. (2015). Cep55 regulates embryonic growth and development by promoting
822   Akt stability in zebrafish. *FASEB J, 29*(5), 1999-2009. doi:10.1096/fj.14-265090
823 Kastenhuber, E. R., & Lowe, S. W. (2017). Putting p53 in Context. *Cell, 170*(6), 1062-1078.
824   doi:10.1016/j.cell.2017.08.028
825 Lafaurie-Janvore, J., Maiuri, P., Wang, I., Pinot, M., Manneville, J. B., Betz, T., Balland, M., & Piel, M.
826   (2013). ESCRT-III assembly and cytokinetic abscission are induced by tension release in the
827   intercellular bridge. *Science, 339*(6127), 1625-1629. doi:10.1126/science.1233866
828 Lee, H. H., Elia, N., Ghirlando, R., Lippincott-Schwartz, J., & Hurley, J. H. (2008). Midbody targeting of
829   the ESCRT machinery by a noncanonical coiled coil in CEP55. *Science, 322*(5901), 576-580.
830   doi:10.1126/science.1162042
831 Lenhart, K. F., & DiNardo, S. (2015). Somatic cell encystment promotes abscission in germline stem
832   cells following a regulated block in cytokinesis. *Dev Cell, 34*(2), 192-205.
833   doi:10.1016/j.devcel.2015.05.003
834 Li, H., Bielas, S. L., Zaki, M. S., Ismail, S., Farfara, D., Um, K., Rosti, R. O., Scott, E. C., Tu, S., Chi, N.
835   C., Gabriel, S., Erson-Omay, E. Z., Ercan-Sencicek, A. G., Yasuno, K., Caglayan, A. O.,
836   Kaymakcalan, H., Ekici, B., Bilguvar, K., Gunel, M., & Gleeson, J. G. (2016). Biallelic
837   Mutations in Citron Kinase Link Mitotic Cytokinesis to Human Primary Microcephaly. *Am J
838   Hum Genet, 99*(2), 501-510. doi:10.1016/j.ajhg.2016.07.004
839 Little, J. N., & Dwyer, N. D. (2019). p53 deletion rescues lethal microcephaly in a mouse model with
840   neural stem cell abscission defects. *Hum Mol Genet, 28*(3), 434-447. doi:10.1093/hmg/ddy350
841 Llorca, A., Ciceri, G., Beattie, R., Wong, F. K., Diana, G., Serafeimidou-Pouliou, E., Fernandez-Otero,
842   M., Streicher, C., Arnold, S. J., Meyer, M., Hippenmeyer, S., Maravall, M., & Marin, O. (2019).
843   A stochastic framework of neurogenesis underlies the assembly of neocortical cytoarchitecture.
844   *Elife, 8*. doi:10.7554/eLife.51381
845 Loo, L., Simon, J. M., Xing, L., McCoy, E. S., Niehaus, J. K., Guo, J., Anton, E. S., & Zylka, M. J.
846   (2019). Single-cell transcriptomic analysis of mouse neocortical development. *Nat Commun,
847   10*(1), 134. doi:10.1038/s41467-018-08079-9
848 Makrythanasis, P., Maroofian, R., Stray-Pedersen, A., Musaev, D., Zaki, M. S., Mahmoud, I. G., Selim,
849   L., Elbadawy, A., Jhangiani, S. N., Coban Akdemir, Z. H., Gambin, T., Sorte, H. S., Heiberg, A.,
850   McEvoy-Venneri, J., James, K. N., Stanley, V., Belandres, D., Guipponi, M., Santoni, F. A.,
851   Ahangari, N., Tara, F., Doosti, M., Iwaszkiewicz, J., Zoete, V., Backe, P. H., Hamamy, H.,
852   Gleeson, J. G., Lupski, J. R., Karimiani, E. G., & Antonarakis, S. E. (2018). Biallelic variants in
853   KIF14 cause intellectual disability with microcephaly. *Eur J Hum Genet.* doi:10.1038/s41431-
854   017-0088-9
855 Mao, H., McMahon, J. J., Tsai, Y. H., Wang, Z., & Silver, D. L. (2016). Haploinsufficiency for Core
856   Exon Junction Complex Components Disrupts Embryonic Neurogenesis and Causes p53-
857   Mediated Microcephaly. *PLoS Genet, 12*(9), e1006282. doi:10.1371/journal.pgen.1006282
858 McNally, F. J., & Roll-Mecak, A. (2018). Microtubule-severing enzymes: From cellular functions to
859   molecular mechanism. *J Cell Biol, 217*(12), 4057-4069. doi:10.1083/jcb.201612104
860 McNeely, K. C., & Dwyer, N. D. (2020). Cytokinesis and postabscission midbody remnants are regulated
861   during mammalian brain development. *Proc Natl Acad Sci U S A, 117*(17), 9584-9593.
862   doi:10.1073/pnas.1919658117
863 Mierzwa, B., & Gerlich, D. W. (2014). Cytokinetic abscission: molecular mechanisms and temporal
864   control. *Dev Cell, 31*(5), 525-538. doi:10.1016/j.devcel.2014.11.006
865 Moawia, A., Shaheen, R., Rasool, S., Waseem, S. S., Ewida, N., Budde, B., Kawalia, A., Motameny, S.,
866   Khan, K., Fatima, A., Jameel, M., Ullah, F., Akram, T., Ali, Z., Abdullah, U., Irshad, S., Hohne,

867   W., Noegel, A. A., Al-Owain, M., Hortnagel, K., Stobe, P., Baig, S. M., Nurnberg, P., Alkuraya,
868   F. S., Hahn, A., & Hussain, M. S. (2017). Mutations of KIF14 cause primary microcephaly by
869   impairing cytokinesis. *Ann Neurol, 82*(4), 562-577. doi:10.1002/ana.25044
870 Morita, E., Sandrin, V., Chung, H. Y., Morham, S. G., Gygi, S. P., Rodesch, C. K., & Sundquist, W. I.
871   (2007). Human ESCRT and ALIX proteins interact with proteins of the midbody and function in
872   cytokinesis. *EMBO J, 26*(19), 4215-4227. doi:10.1038/sj.emboj.7601850
873 Muzumdar, M. D., Tasic, B., Miyamichi, K., Li, L., & Luo, L. (2007). A global double-fluorescent Cre
874   reporter mouse. *Genesis, 45*(9), 593-605. doi:10.1002/dvg.20335
875 Paradis, A. N., Gay, M. S., & Zhang, L. (2014). Binucleation of cardiomyocytes: the transition from a
876   proliferative to a terminally differentiated state. *Drug Discov Today, 19*(5), 602-609.
877   doi:10.1016/j.drudis.2013.10.019
878 Peterman, E., Gibieza, P., Schafer, J., Skeberdis, V. A., Kaupinis, A., Valius, M., Heiligenstein, X.,
879   Hurbain, I., Raposo, G., & Prekeris, R. (2019). The post-abscission midbody is an intracellular
880   signaling organelle that regulates cell proliferation. *Nat Commun, 10*(1), 3181.
881   doi:10.1038/s41467-019-10871-0
882 Pollarolo, G., Schulz, J. G., Munck, S., & Dotti, C. G. (2011). Cytokinesis remnants define first neuronal
883   asymmetry in vivo. *Nat Neurosci, 14*(12), 1525-1533.
884 Rawlins, L. E., Jones, H., Wenger, O., Aye, M., Fasham, J., Harlalka, G. V., Chioza, B. A., Miron, A.,
885   Ellard, S., Wakeling, M., Crosby, A. H., & Baple, E. L. (2019). An Amish founder variant
886   consolidates disruption of CEP55 as a cause of hydranencephaly and renal dysplasia. *Eur J Hum
887   Genet, 27*(4), 657-662. doi:10.1038/s41431-018-0306-0
888 Ren, H. P., & Russell, L. D. (1991). Clonal development of interconnected germ cells in the rat and its
889   relationship to the segmental and subsegmental organization of spermatogenesis. *Am J Anat,
890   192*(2), 121-128. doi:10.1002/aja.1001920203
891 Said Halidi, K. N., Fontan, E., Boucharlat, A., Davignon, L., Charpentier, M., Boulle, M., Weil, R., Israel,
892   A., Laplantine, E., & Agou, F. (2019). Two NEMO-like Ubiquitin-Binding Domains in CEP55
893   Differently Regulate Cytokinesis. *iScience, 20*, 292-309. doi:10.1016/j.isci.2019.08.042
894 Singh, D., & Pohl, C. (2014). A function for the midbody remnant in embryonic patterning. *Commun
895   Integr Biol, 7*, e28533. doi:10.4161/cib.28533
896 Skop, A. R., Liu, H., Yates, J., 3rd, Meyer, B. J., & Heald, R. (2004). Dissection of the mammalian
897   midbody proteome reveals conserved cytokinesis mechanisms. *Science, 305*(5680), 61-66.
898 Steigemann, P., Wurzenberger, C., Schmitz, M. H., Held, M., Guizetti, J., Maar, S., & Gerlich, D. W.
899   (2009). Aurora B-mediated abscission checkpoint protects against tetraploidization. *Cell, 136*(3),
900   473-484.
901 Stoten, C. L., & Carlton, J. G. (2018). ESCRT-dependent control of membrane remodelling during cell
902   division. *Semin Cell Dev Biol, 74*, 50-65. doi:10.1016/j.semcdb.2017.08.035
903 Tedeschi, A., Almagro, J., Renshaw, M. J., Messal, H. A., Behrens, A., & Petronczki, M. (2020). Cep55
904   promotes cytokinesis of neural progenitors but is dispensable for most mammalian cell divisions.
905   *Nat Commun, 11*(1), 1746. doi:10.1038/s41467-020-15359-w
906 Van de Putte, T., Zwijsen, A., Lonnoy, O., Rybin, V., Cozijnsen, M., Francis, A., Baekelandt, V., Kozak,
907   C. A., Zerial, M., & Huylebroeck, D. (2001). Mice with a homozygous gene trap vector insertion
908   in mgcRacGAP die during pre-implantation development. *Mech Dev, 102*(1-2), 33-44.
909   doi:10.1016/s0925-4773(01)00279-9
910 Visel, A., Thaller, C., & Eichele, G. (2004). GenePaint.org: an atlas of gene expression patterns in the
911   mouse embryo. Nucleic Acids Res, 32(Database issue), D552-556. doi:10.1093/nar/gkh029
912 Yanagi, K., Sone, R., Ohga, R., & Kawahara, A. (2019). Involvement of the centrosomal protein 55
913   (cep55) gene in zebrafish head formation. *Genes Cells, 24*(10), 642-649. doi:10.1111/gtc.12715
914 Zhao, W. M., Seki, A., & Fang, G. (2006). Cep55, a microtubule-bundling protein, associates with
915   centralspindlin to control the midbody integrity and cell abscission during cytokinesis. *Mol Biol
916   Cell, 17*(9), 3881-3896.
917